ENHANCEMENT OF LIGHT TRAPPING IN THIN FILM SILICON SOLAR CELLS

MASTERS THESIS

FROM

LU ZHAO

BORN ON THE 9TH OF APRIL 1985 IN BEIJING, CHINA

SEPTEMBER 2, 2009

SUPERVISORS:
PROF. MIRO ZEMAN
IR. KLAUS JÄGER

TECHNISCHE UNIVERSITEIT DELFT
FACULTY OF APPLIED SCIENCE
PROGRAMME OF SUSTAINABLE ENERGY TECHNOLOGY

Abstract

Recently photovoltaic techniques have drawn extensive attention both in research and industry. Thin film silicon solar cells are becoming more promising due to their low material and energy consumption, when compared to wafer-based crystalline silicon solar cells. However, the efficiency of thin film solar cells is still relative low. Light trapping is one of the approaches through which the efficiency can be considerably improved.

To achieve light trapping in the thin film silicon solar cells, rough surfaces presented on transparent conductive oxide (TCO) are included, either on top of or at the bottom of solar cells. The rough surface enables strong light scattering which enhances the absorption in the thin absorptive layers. In this way the short circuit current can be improved as well as the efficiency. In this thesis, we investigated three types of TCOs, including fluorine doped tin oxide (FTO), aluminum doped zinc oxide (AZO) and boron doped zinc oxide (BZO). Light scattering properties of these TCOs and their surface morphologies were studied.

Morphological and optical measurements were carried out to determine surface root-mean-square (rms) roughness, haze and angular distribution functions (ADFs). The results showed that with an increased surface rms roughness, an enhancement in light scattering was observed. This effect becomes more pronounced especially when the rms roughness is comparable to the shorter wavelength, i.e. in ultraviolet/visible region. However, it is found that rms roughness could not completely describe the scattering behaviors, the lateral features are also required. In particular, pyramidal structures are more likely to scatter light into angles close to the surface normal, while crater-like surface structures are more favorable into angles out of the incident light direction. With a better theoretical understanding of the scattering behaviors, one can propose optimized surface structures for future manufacturing process.

Contents

Chapter 1

Introduction

1.1 Background and motivation

With global warming and energy conservation becoming a critical focus, the need to reduce the world's reliance on fossil fuel is being concerned with great urgency. By the year 2030, the worldwide energy consumption is projected to increase by 44% [1]. To satisfy such a rapid growing demand, several energy source alternatives, including wind, biomass, hydropower, geothermal, tidal and solar energy, have been pushed out to accelerate the transition towards a renewable and sustainable society. Continuous increasing fossil fuel prices, especially for oil and natural gas, along with government policies and programs supporting renewable energy, will allow renewable fuels to compete more economically in the near future.

Solar energy provides a clean solution to achieve long-term sustainability of energy consumption. Photovoltaic (PV) solar technique, which directly converts sunlight into electricity, is proven to be the only renewable energy technology available now, since it generates electricity through a renewable source, and has no barriers for installation. Additionally, it does not emit any greenhouse gases and is almost maintenance free. According to the PV market report in 2008 [2], the cumulative global production of PV systems reached 12.4 GW at the end of 2007. The cost of PV modules has fallen considerably in the last two decades, but since 2004 this trend has no longer occurred as expected due to insufficient production of suitable silicon [3], which led to additional manufacturing cost of PV modules such as wafer silicon solar cells. To drive the module cost down further, wafer silicon alternatives have to be employed.

Thin film silicon photovoltaics, i.e. amorphous (a-Si), microcrystalline (μc-Si) and 'micromorph' (a-Si/μc-Si) tandem silicon solar cells, represent promising candidates for future photovoltaic energy conversion, due to their low material consumption and moderate temperature processing, which shortens the energy pay back time and reduces the manufacturing cost substantially. Additionally, this kind of solar cells can be deposited on more cost-effective substrate materials, either rigid or flexible, such as glass, stainless steel and plastics. Further, they can be integrated onto windows and roofs, and adapted to applications varied from the mW to MW ranges, such as portable calculators, toys and large power plants. However, current thin film solar cells are still limited to relative low efficiencies when compares with wafer silicon cells, and for *a*-Si cells they are not stable initially due to the light-induced degradation. These are the main issues many researchers have been working on recent years in the thin film silicon solar cell field.

Light trapping technique is an attractive approach that help improve the solar cell efficiency. To achieve this one possible way is to scatter light at rough interfaces. The rough surface structure within the cell layers can be done by introducing roughness to the front transparent conductive oxide (TCO) layer, or back reflector layer of the solar cell. Light scattering can be enhanced in this way and subsequently the overall efficiency. This thesis is aiming at investigating various TCO layers, from both optical and morphological aspects, and searching for the theoretical connection between the rough surface structures and their optical properties. With a better theoretical understanding one can propose optimized surface structures for future manufacturing process.

1.2 Thin-film silicon solar cells

1.2.1 Historical review

Silicon is an abundant, non-toxic, semiconducting material. It can be modified from its purest, single crystalline phase, to an almost perfectly disordered, amorphous phase. A mixed phase of the two is namely microcrystalline or nanocrystalline. Shortly after Spear and Le Comber [4] reported that *a*-Si can also be doped *n*-type or *p*-type by glow discharge deposition in 1975, the first thin-film *a*-Si solar cell was developed by RCA Laboratories with an energy conversion efficiency of 2.4% [5]. At around that time, the fact that hydrogen played an important role in the newly doped films was recognized [6], therefore amorphous silicon is actually an alloy of silicon and hydrogen, namely hydrogenated amorphous silicon (*a*-Si:H).

The successful doping of amorphous silicon also triggered the researches on microcrystalline silicon. In 1979 and 1980, hydrogenated microcrystalline silicon (μc-Si:H) films were made with high hydrogen dilution regime through glow discharge deposition [7,8], and these films were applied in *p*-*i*-*n* solar cell in 1987 [9]. In 1994, IMT Neuchâtel succeeded in preparing a fully μc-Si:H *p*-*i*-*n* single junction solar cell with an efficiency of 4.6% [10]. For *a*-Si solar cell, stablized efficiency up to 9.47% has been reported by IMT Neuchâtel [11], while for μc-Si:H solar cell, Kaneka still kept the record of 10.1% [12,13].

The development of μc-Si:H opens up new ways for thin-film multi-junction solar cells, the most promising one being the 'micromorph' tandem solar cell. This type of cell consists of an a-Si:H top cell and a μc-Si:H bottom cell and with the combination of two p-i-n junctions the solar spectrum can be utilized more efficiently, compensated for the losses due to thermalization. Moreover, the relative instability of a-Si:H cell can be moderated due to this combination. An initial efficiency of 14.1% has been achieved for a-Si:H/transparent interlayer/poly Si solar cell [14] and for μc-Si:H thin submodule 11.7% was reported by Kaneka [13,15]. For micromorph tandem cell, IMT Neuchâtel reported their highly stable performed test cell with an intermediate ZnO reflector layer, an stablized efficiency of 10.7% [11].

1.2.2 Structure and properties

A typical thin-film solar cell is constituted of a boron-doped p-layer, an intrinsic (i-) layer and an phosphorous-doped n-layer that formed within the same semiconducting material, and then sandwiched between a front electrode (normally TCO layer) and a back electrode (either TCO and/or a metallic contact). The basic principle of a photovoltaic conversion is the generation of electron-hole pairs in the absorber when photons strike on the solar cell. The electron-hole pairs are then separated due to internal electric field that provided by n-layer and p-layer, and collected at the electrodes at both sides, finally a current or voltage is gained in an external circuit.

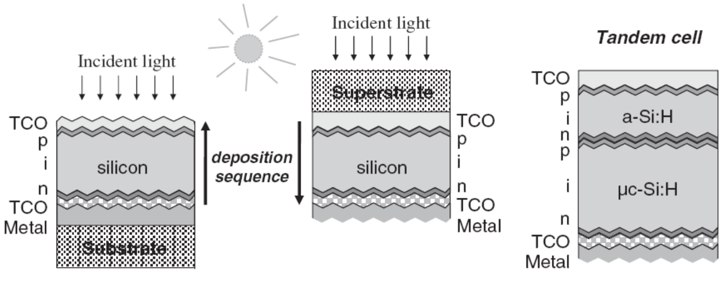

Figure 1.1: Structure of single junction substrate, superstrate and an amorphous/microcrystalline tandem solar cells [16].

Generally, a cell is either p-i-n (superstrate) or n-i-p (substrate), depending on the deposition sequence of doped and intrinsic layers. Both configurations allow light enters through the p-layer. The reason for this is that most charged carriers are generated at a closer location to the p-layer, in order to let the lower-mobility holes be collected more efficiently, the distance holes need to travel should be shortened, thus p-layer is situated at the illuminated side. An a-Si solar cell is in the order of several hundreds of nanometers thick, while the doped layers are only 10-30 nm thick. The entire cell thickness needs to be balanced between not to extremely reduce the amount of light it can absorbs (when it is rather thin) and not to weaken the intensity of internal electric field (when it is rather thick). One may enhance the electric field through high concentration doping, but this will introduce more trapping centers in the *i*-layer, leading to carrier recombination instead of being collected. Two solution might be feasible to solve the problem, one is through multi-junction (tandem) concept, which can reduce the degradation effect while maintain the cell thick enough, or the other one, through light trapping, to increase the optical path of light while keeping the cell thin. Figure 1.1 gives a sketch for substrate, superstrate single junction solar cell and a tandem solar cell.

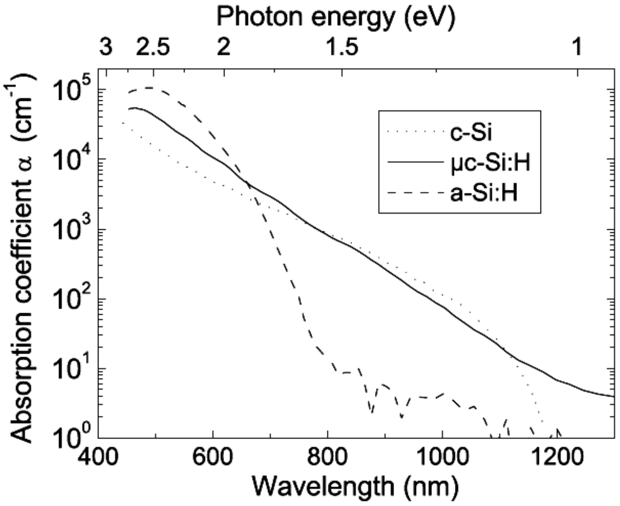

Figure 1.2: Absorption coefficient α of *a*-Si:H (dashed), *μc*-Si:H (solid) and *c*-Si (dotted) as a function of wavelength (nm) and photon energy (eV) [17].

The most important electrical property of doped thin films is the conductivity, while the most important optical property is the absorption coefficient. Good doped layers should have both high conductivity, to lower the electrical load, and good optical transparency, not to absorb light. The absorption coefficients α of typical *a*-Si:H, *μc*-Si:H and *c*-Si are shown in Figure 1.2. Standard *a*-Si:H has a optical bandgap around 1.7-1.8 eV, and exhibits a high absorption coefficient over almost whole visible spectrum region. Compared to *a*-Si:H, the *μc*-Si:H has a lower bandgap at around 1.1 eV, and shows the potential of using the near infrared (NIR) spectrum up to 1100 nm. With a combination of the two, a better utilization of the solar spectrum is achieved. This can also be proved in quantum efficiency (QE), which gives the fraction of incident photons that contributes to the photo current generation, as shown in Figure 1.3. The figure illustrates how *a*-Si:H be active in the visible light region while *μc*-Si:H extends the absorption range further to the NIR region, but there is still some broad potential for further improvement.

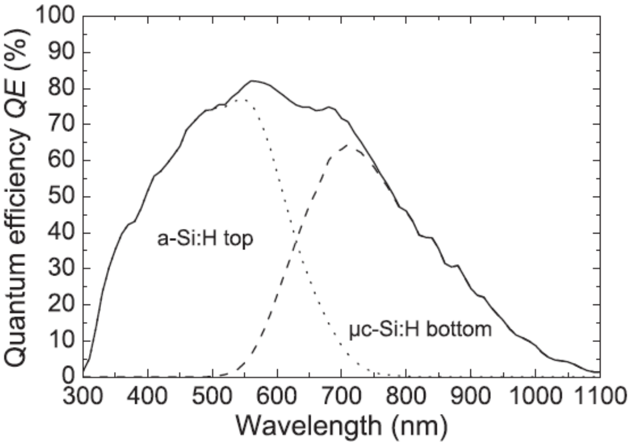

Figure 1.3: Quantum efficiency of *a*-Si:H (dotted), *μc*-Si:H (dashed) and *a*-Si:H / *μc*-Si:H tandem solar cells as a function of wavelength (nm) [16].

As mentioned previously, the light-induced degradation will affect the performance of *a*-Si:H solar cells. The defects generated in the *i*-layer are referring to the dangling bonds of the silicon atoms, which act as trapping centers for electron and hole carriers. This results in a decrease in the electric field and consequently the value of V_{oc} and the efficiency. Although most of the dangling bonds can already be saturated by adding 10% of hydrogen, they are not permanently stable, the bonds can broke again by the capture of holes, leading to continuous degradation of the cell [18]. Meier et al. [19] has reported that for a *p*-*i*-*n* struture cell with an *i*-layer around 250 nm thickness, the efficiency will drop by approximately 15% until it reaches stablized state. In comparison to *a*-Si:H, *μc*-Si:H is much more stable to light exposure [10]. The reason in detail is described in the reference papers [10,20,21]. With a proper combination, the efficiency degradation of micromorph tandem cell can be limited to less than 10% relative [16].

1.3 Light loss and trapping in thin-film silicon solar cells

1.3.1 Light loss in the front and back contact

The light loss in thin-film silicon solar cells mainly attributes to the spectral mismatch, the reflection at the front contact and transmission at the back contact, which in total takes up two thirds of the entire loss. In case of a superstrate configuration, incident light that can not reach the *p*-layer leads to reflection loss, the light with relative larger wavelength ($\geq$ 650 nm) just pass through the very thin silicon layers and part of them then pass through the back contact, leads to transmission loss. In both circumstances, large fraction of light does not take part in the photovoltaic process. While the reflectance at the front is more or less wavelength independent, the transmission loss at the back is strongly wavelength dependent. Tao [22] proposed a 13.1% loss at the front contact based on a glass/TCO/*p*-*a*-Si:H structure. For a 500 nm thick *a*-Si:H layer, the transmission loss can be up to 9.5% and 21% for 650 nm and 700 nm wavelength light based on a *n*-*a*-Si:H/Al structure, and reduces to 4.7% and 11% at these wavelengths if aluminum back contact is replaced with a silver one.

As already shown in Figure 1.2, both *a*-Si:H and μc-Si:H exhibit poor absorption coefficients upon spectrum wavelength larger than 800 nm. Although the relative low bandgap allows μc-Si:H to have extensional absorption up to the near infrared region, the indirect property of its bandgap still limit the absorption at this region. This illustrates the necessity of light trapping particularly for long wavelengths.

1.3.2 Light trapping theory and method

The spectral mismatch problem can be improved through building up multijunction cells, as already mentioned previously. In order to keep the cell thickness reasonable low, the reflection and transmission loss can only be minimized by optical means, for instance, by light trapping. The effect of light trapping inside a semiconductor by total internal reflection was first observed in 1965 [23]. The reflectivity of a body will decrease when the reflected photons are deflected and hit on the body a second time. As the photons are reflected back and forth between bottom and top contact and experience an additional absorption during every pass. This leads to a prolonged path of the photons within the body and therefore an considerable gain in absorptivity. Extensive researches have been done to prove that the short circuit current density J_{sc} of solar cell can be increased through light trapping [24, 25].

Light trapping technique has been implemented in several ways. It can be done through the use of TCO with high surface roughness, to have more light scattering within the structure; or through a textured back reflector, to reuse the reflected photons and further increase the optical path of light. The theoretical maximum enhancement factor for the optical for the optical path length is $4n^2$, where n is the real part of the refractive index of the medium [26]. In case of *a*-Si:H with $n \approx 3.5$, a factor more than 40 should be achieved in theory. However, in practice, only a factor of 5 is determined experimentally [27]. Moreover, The reflection at the front contact can also be reduced through anti-reflection coating. Meier et al. [11] has reported that based on a glass/ZnO/*p*-*a*-Si:H structure, an anti-reflective (AR) layer coated on the front glass side can further decrease the reflectance by approximately 4%, therefore keep the reflection loss at a rather low level. In case of a micromorph cell, light trapping can be improved through an intermediate reflector between top a-Si:H cell and bottom μc-Si:H cell [14]. This interlayer has a different refractive index thus is able to modify the direction of the light going towards the bottom cell, let the light be absorbed more efficiently. In this thesis, we only focus on the light trapping enhancement through the use of textured or rough TCOs.

1.4 Outline and scope of this thesis

This thesis is structured in the following way. First, a general introduction of thin-film silicon solar cell, the light trapping theory and methods will be given in Chapter One. In Chapter Two, basic optics will be described, in order to provide enough background for further chapters. This is followed by the introduction of three characterization techniques used in this study, including Integrating Sphere, Automated Reflectance Transmittance Analyzer and Atomic Force Microscope. Chapter Three will briefly describe the electrical and optical properties of TCO films (in particular, fluorine doped tin oxide (SnO_2:F), aluminum doped zinc oxide (ZnO:Al) and boron doped zinc oxide (ZnO:B)). Experimental part are also explained in this chapter. The results upon TCOs' scattering properties will be explored in Chapter Four. With measurements performed through different techniques, results of each sample are discussed in this chapter. Finally, conclusions will be drawn in Chapter Five. Various try-out measurements performed by ARTA will be included in the Appendix.

Chapter 2

Characterization techniques

In this Chapter, some basic optics of light behavior are briefly described. This is followed by the introduction of three characterization techniques, including a spectrometer, and its two accessories, an Integrating Sphere (IS), the Automated Reflectance Transmittance Analyzer (ARTA), and Atomic Force Microscopy (AFM). IS and ARTA are used for characterizing the far-field optical properties of various TCOs, while AFM is used to characterize and analyze the morphology of flat/rough surfaces of these TCOs.

2.1 General optics

This section will briefly go through some basic optical theories in terms of their mathematical expressions, aiming to gain a better understanding of how light propagates and behaves in different medium.

2.1.1 Spectrum

At the beginning, spectra description in terms of their names, abbreviations and wavelengths (λ) are listed in Table 2.1.

2.1.2 Transmission, reflection and absorption

When light is incident on a rough material, several things may occur, it is either *specularly transmitted* or *diffusely transmitted* through the sample, or *specularly reflected* from the sample, or *diffusely scattered* at the sample surface or in its volume, or *absorbed* within the sample. The total *transmittance* T of a sample is defined as the ratio of the intensity of transmitted light I_T and that of the incoming light I_0, or the sum of *specular transmittance* T_{spec} and *diffuse transmittance* T_{diff}, as shown in following equations:

Table 2.1: List of spectrum wavelengths

Name of spectrum	Abbrev.	λ (nm)
Ultraviolet	UV	**10 - 400**
Near ultraviolet	NUV	300 - 400
Visible	Vis	**380 - 750**
Violet		380 - 450
Blue		450 - 495
Green		495 - 570
Yellow		570 - 590
Orange		590 - 620
red		620 - 750
Near infrared	NIR	**750 - 1400**
Infrared	IR	**1400 - 10^6**

$$T \equiv \frac{I_T}{I_0} \tag{2.1}$$

$$T = T_{\text{spec}} + T_{\text{diff}} \tag{2.2}$$

Similarly, the total *reflectance* R is given by the ratio of the transmitted light intensity I_R to the incoming light intensity I_0, or the sum of *specular reflectance* R_{spec} and *diffuse reflectance* R_{diff}, as shown in following equations:

$$T \equiv \frac{I_R}{I_0} \tag{2.3}$$

$$R = R_{\text{spec}} + R_{\text{diff}} \tag{2.4}$$

The *absorptance* A is expressed in terms of the ratio of the absorbed light intensity I_A and the incoming light one I_0, which is:

$$A = \frac{I_A}{I_0} \tag{2.5}$$

According to the energy conservation law, these components must sum up to value one:

$$T + R + A = 1 \tag{2.6}$$

All these values are dependent on the wavelength of the light.

There is a further concept describing optical sample properties called *absorbance* $\mathcal{A}$, which may directly be obtained by means of spectrophotometer, that measures the ratio between the sample transmittance T and that of the reference T_{ref}. From this, the absorbance can be calculated as:

$$\mathcal{A} \equiv -\lg \frac{T}{T_{\mathrm{ref}}} \tag{2.7}$$

The most important optical property of thin films is the *absorption coefficient* α, as described in the Lambert-Beer law:

$$I = I_0 e^{-\alpha x} \tag{2.8}$$

Where I is the light intensity transmit through a layer of material with thickness x, with respect to the incident light intensity.

2.1.3 Refractive index, dispersion, Snell's law, polarization and Fresnel's equations

When light transmits through an interface between two different transparent media at an angle, either specularly or diffusely, it must be refracted. Each medium may be characterized with an *Refractive index* (or *Index of refraction*) n, which is a parameter describing the reduction of light velocity inside the medium compared with in vacuum, i.e. $n = c \,/\, v$, where c is light velocity in vacuum. The refractive index of air is arbitrarily taken to be 1, and for typical TCO for example zinc oxide $n \approx 2.3$. Both n and v are dependent on wavelength, as n slightly increases with decreasing wavelength near the absorption edge [28], the shorter wavelength light will travel slower within this medium. This phenomenon is known as *dispersion*.

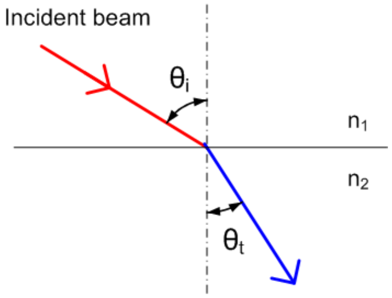

Figure 2.1: Refraction at an interface.

Snell's law describes the relationship between angles of incident and refracted light at an interface of two media with different refractive index, as expressed in Equation 2.9.

$$\frac{\sin\theta_{\mathrm{i}}}{\sin\theta_{\mathrm{t}}} = \frac{n_2}{n_1}, \tag{2.9}$$

where θ_i is the angle between incident beam and normal, and θ_t is the angle between transmitted beam and normal. n_1 and n_2 are the refractive indices for the first and second medium, respectively, as shown in Figure 2.1.

The optical properties of specular materials depend on the polarization of light, except the case of normal incidence. Polarization is a property of light that describes the orientation of its oscillation. Since light is electromagnetic wave, the polarization is determined by specifying the direction of wave's electric field. The plane that contains incident, reflected and refracted waves is known as the incidence plane. P-polarization is defined when the direction of electric field is parallel to the incidence plane, while s-polarization means electric field is perpendicular to the incidence plane.

Fresnel's equations describe the behavior of light traveling between media with different refractive indices. The relationship among the intensity of incident beam, reflected beam and refractive beam, depends on the incident angle, the refractive index of material, and the polarization. For p-polarization, the expressions for transmission coefficient (t_p) and reflection coefficient (r_p) are given in Equation 2.10 and 2.11, and for s-polarization, transmission and reflection coefficient (t_s and r_p) are given in Equation 2.12 and 2.13 [29].

For p-polarization:

$$t_p = \left(\frac{E_{ot}}{E_{oi}}\right)_{\parallel} = \frac{2\tilde{n}_1 \cos\theta_\mathrm{i}}{\tilde{n}_2 \cos\theta_\mathrm{i} + \tilde{n}_1 \cos\theta_\mathrm{t}}, \tag{2.10}$$

$$r_p = \left(\frac{E_{or}}{E_{oi}}\right)_{\parallel} = \frac{\tilde{n}_2 \cos\theta_\mathrm{i} - \tilde{n}_1 \cos\theta_\mathrm{t}}{\tilde{n}_2 \cos\theta_\mathrm{i} + \tilde{n}_1 \cos\theta_\mathrm{t}}, \tag{2.11}$$

For s-polarization:

$$t_s = \left(\frac{E_{ot}}{E_{oi}}\right)_{\perp} = \frac{2\tilde{n}_1 \cos\theta_\mathrm{i}}{\tilde{n}_1 \cos\theta_\mathrm{i} + \tilde{n}_2 \cos\theta_\mathrm{t}}, \tag{2.12}$$

$$r_s = \left(\frac{E_{or}}{E_{oi}}\right)_{\perp} = \frac{\tilde{n}_1 \cos\theta_\mathrm{i} - \tilde{n}_2 \cos\theta_\mathrm{t}}{\tilde{n}_2 \cos\theta_\mathrm{i} + \tilde{n}_1 \cos\theta_\mathrm{t}}, \tag{2.13}$$

where E_o is the electric field amplitude of waves that corresponds to transmission or reflection coefficients, and subscripts t, r and i denote the transmitted (or refracted), reflected and incident beam, respectively.

The reflectance of p- and s-polarized light (R_p and R_s) can be calculated, since the intensity is proportional to the square of the modulus of the electric field amplitude.

$$R_p = \left[\frac{\tilde{n}_2 \cos\theta_\mathrm{i} - \tilde{n}_1 \cos\theta_\mathrm{t}}{\tilde{n}_2 \cos\theta_\mathrm{i} + \tilde{n}_1 \cos\theta_\mathrm{t}}\right]^2 \tag{2.14}$$

$$R_s = \left[\frac{\tilde{n}_1 \cos\theta_\mathrm{i} - \tilde{n}_2 \cos\theta_\mathrm{t}}{\tilde{n}_2 \cos\theta_\mathrm{i} + \tilde{n}_1 \cos\theta_\mathrm{t}}\right]^2 \tag{2.15}$$

And

$$R = |r|^2 \tag{2.16}$$

In case of normal incidence and purely real refractive indices, we have

$$R = \left(\frac{n_1 - n_2}{n_1 + n_2}\right)^2 \tag{2.17}$$

There is a particular angle of incidence, namely *Brewster's angle* (θ_B), where p-polarized light disappears ($r_p = 0$) and only s component is reflected. At this angle, the reflected and refractive waves propagate at right angles to one another, as shown in Figure 2.2. The Brewster's angle can be determined through Equation 2.18. For an air/TCO ($n \approx 2.3$) interface, $\theta_\mathrm{B} \approx 67^\circ$.

$$\theta_\mathrm{B} = \arctan\frac{n_2}{n_1} \tag{2.18}$$

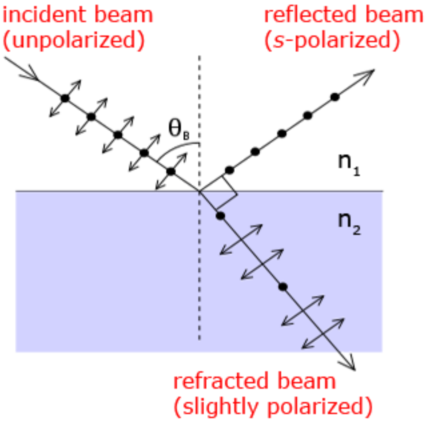

Figure 2.2: Brewster's angle. The parallel arrows and spots indicate the directions of wave's magnetic field and electric field, respectively.

Figure 2.3 shows the transmittance and reflectance of 500-nm light passing through glass with different polarization states as a function of the angle of incidence. The difference given by p- and s-polarization can be significant near the Brewster's angle. In our measurements, only p-polarized light is used. For oblique incidence, a reduction of transmitted light intensity may be detected at specific wavelength.

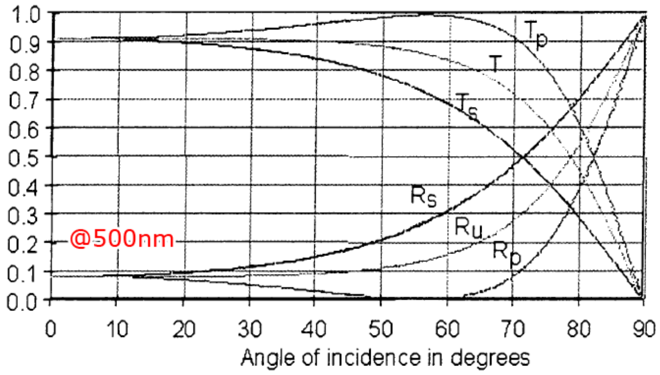

Figure 2.3: Directional transmittance (T) and reflectance (R) of a 4 mm clear float glass at wavelength of 500 nm. The subscripts S, P and U refer to the *S*-polarized, *P*-polarized and unpolarized (natural light), respectively [30].

2.1.4 Interference and diffraction

Interference occurs when several beams interact, and *diffraction* occurs when light waves interact with a single aperture. If there are several apertures, then a spreading of waves will occur. At the place far from the apertures, diffracted waves overlap with one another, and this leads to an *interference pattern.*

In principle, diffraction is observed when light is restricted by an opening or sharp edge, no matter how large it is. However, diffraction is most pronounced for waves where the wavelength is on the order of the dimension of the diffracting objects. Consider a plane surface on top of which many small facets are randomly distributed and oriented in various directions [31]. If the dimension of these facets are large compared with the wavelength of light, the reflected or refracted waves will take each facet as an individual surface, so that they are determined entirely by the geometry of these facets. As the wavelength becomes longer, more comparable with the size of facet, diffraction will become more dominant than their geometries. When the wavelength becomes much longer so that facets are very small by comparison, the reflected or refracted waves will be determined totally by diffraction, and these relative small features can be seen as a group of apertures on the plane surface. In our case, the geometry of facets is described as inclination, or more particularly, the root mean square slope of the surface irregularities. And the dimension of facets is mainly referred to the root mean square roughness (σ_{rms}) of the surface irregularities (will be further explored in this chapter, Section 2.3).

2.1.5 Solid angle

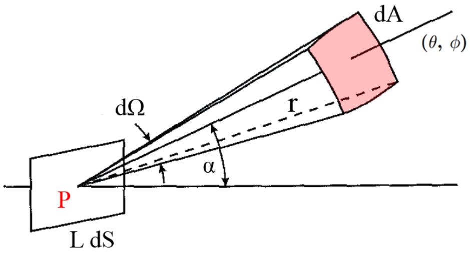

Figure 2.4: Schematic definition of solid angle and the radiance of a small plane area [28].

Solid angle (Ω) is an angle element extended in three dimensional space (see Figure 2.4). Consider an object placed in the center of a sphere, solid angle is determined as the surface area A of this object's projection onto the sphere, divided by the square of the sphere's radius R, as expressed in Equation 2.19 [28]. A full sphere subtends a solid angle of 4π *steradians* (sr).

$$\Omega = \frac{A}{R^2} \tag{2.19}$$

The radiant power $\mathrm{d}F$ which is emitted from a point source with a *radiant intensity* I is defined as:

$$\mathrm{d}F = I\mathrm{d}\Omega \tag{2.20}$$

For small plane source, the radiant power $\mathrm{d}F$ emitted from a point P on the surface of element $\mathrm{d}S$ and falls within an element $\mathrm{d}\Omega$ of solid angle around a direction specified by the polar coordinates (θ, ϕ) may be expressed as [28, 32]:

$$\mathrm{d}F = L\mathrm{d}S\cos\alpha\mathrm{d}\Omega, \tag{2.21}$$

where α is the angle between the direction of the line joining $\mathrm{d}S$ and $\mathrm{d}A$ (θ, ϕ) and the normal to the surface element $\mathrm{d}S$, and L is *radiance* at point P on a surface element into direction (θ, ϕ).

2.2 Spectrophotometer

In this study, a *PerkinElemer*® *Lambda*™ *950 Spectrophotometer*, assisted with its two compartments, an *Integrating Sphere* (IS) and the *Automated Reflectance Transmittance Analyzer* (ARTA), are used to perform optical measurements. The spectrophotometer is equipped with a deuterium arc lamp and a tungsten-halogen lamp, with which a wavelength range between 175 nm and 3300 nm is covered. The lamps switch at around 860 nm, which is also the weakest region for the detectors connected to IS and ARTA.

Figure 2.5: The photograph of Integrating Sphere (IS) installed in the *PerkinElemer*$^{\circledR}$ *Lambda*$^{\text{TM}}$ *950 Spectrophotometer.*

2.2.1 Integrating Sphere (IS)

Integrating sphere is used to collect light from a wide range of angles, as shown in Figure 2.5. A diameter of 150 mm allows a low port fraction (around 2.5%) over the entire internal surface area. The large surface area ensures that the incident light is homogeneous along the sphere's surface before it reaches the detector, thereby increases measurement accuracy. Through *Lambda*$^{\text{TM}}$ IS setup, the wavelength dependent optical parameters, total transmittance T_{tot}, diffuse transmittance T_{diff}, total reflectance R_{tot} and diffuse reflectance R_{diff}, can be determined. Two *Spectralon*$^{\text{TM}}$ blanking plates are fitted to the reflectance sample holder (when measuring the transmittance) and reference port. The reference reflectance is taken to be 100% in the entire wavelength range. For very flat samples, *Spectralon*$^{\text{TM}}$ is replaced by a mirror standard from TNO Company. in order to enhance the signal-to-noise ratio. T_{tot} is measured by letting incident light first pass through the glass side of sample layer, enter the sphere from the front opening, and then reach the end of sphere where the reference plate is placed. While T_{diff} is obtained by removing the plate where specular component can leave the sphere. Similarly, R_{tot} is measured by putting the sample at the reference port (glass side outwards), and let incident beam enter the sphere and hit the sample at the end of sphere. Note that the reflectance is obtained at a near normal incidence angle, i.e. 5° apart from normal, in order to avoid reflected light interfered with the incoming light. As a matter of this, R_{diff} can be measured by openning a port 5° near the port where light enters, to make sure the specular component goes away.

The cross section of IS setups are llustrated in Figure 2.6. These values are obtained spatially, as the IS enables light collection over the whole solid angle region. Specific user interface *UWinLAB* was used for measurement parameters setup, data recording and analysis. Various wavelength ranges were chosen for analysis in this thesis, depending on the interesting region of particular TCO samples.

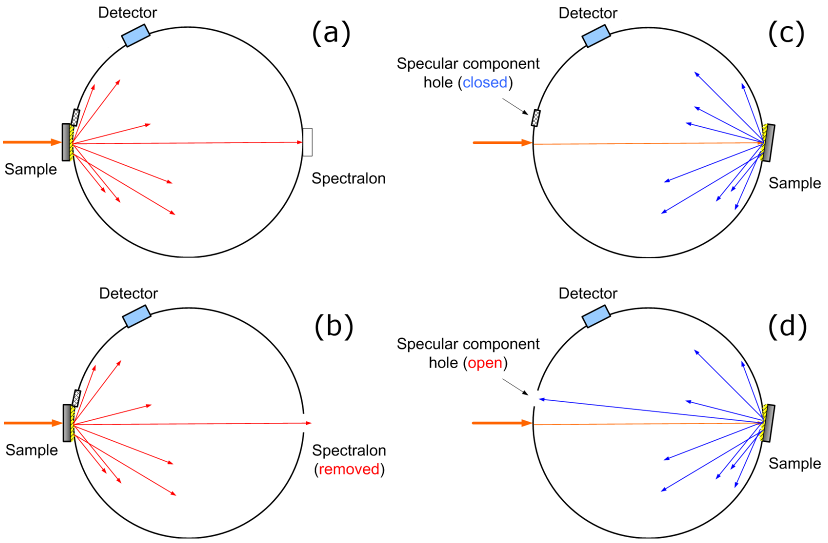

Figure 2.6: Schematic cross section of IS along the measuring plane. The measuring setups of T_{tot}, T_{diff}, R_{tot} and R_{diff} are shown in subgraph (a), (b), (c) and (d), respectively.

The ability of a TCO layer to scatter light is often characterized by the haze parameter, which is defined as ratio of the diffuse component over the total component.

$$H_T = \frac{T_{\text{diff}}}{T_{\text{tot}}} \tag{2.22}$$

$$H_R = \frac{R_{\text{diff}}}{R_{\text{tot}}} \tag{2.23}$$

Since the sample surface may not be ideally homogeneous, it is important to measure the total or diffuse transmittance and reflectance at the same spot on the sample. For haze parameters, noticeable interference may occur if deviation of measuring position (hence deviation in sample thickness) is not taken into account, especially for small roughness samples [33]. We tried to keep the position in the center of sample each time, to minimize the interference pattern for relative flat samples.

2.2.2 Automated Reflectance Transmittance Analyzer (ARTA)

Variable Angle Spectroscopy (VAS) has become a valuable technique for thin film spectral analysis, due to its ability of reducing systematic errors for spectral measurements [34]. Automated Reflectance Transmittance Analyzer (ARTA) [30], which was developed by TNO a few years ago, is one of the instruments using VAS technique. The angular distribution functions (ADFs) of scattered light, which is another important parameter we used to describe scattering properties, can be determined through ARTA. The main component of ARTA is a rotating detector mounted inside a cylindrical shaped chamber. A small integrating sphere is used in the detector, to make the measuring more accurate. The sphere is equipped with a photomultiplier covering the UV/Vis spectrum region and a Peltier cooled PbS cell (IR sensor) for the NIR region. The entire detector is mounted in a large drum that is connected with a stepper motor, which allows the detector rotating in a horizontal plane from 15° to 345° (0° position is defined as the direction where light enters), as shown in Figure 2.8. The detector has a rectangular entrance port 17 mm in height (H) and with an adjustable width (W) up to 30 mm. The sample is vertically fixed in the sample holder in the center of chamber. The sample holder can rotate between 0° and 180°, which allows a wide range of incident angles for measurements. User interface *MAC2000* together with *UWinLAB* were used for setting up, controlling parameters and recording, analyzing data.

Figure 2.7: The photograph of Automated Reflectance Transmittance Analyzer (ARTA) installed in the *PerkinElemer*® *Lambda*™ *950 Spectrophotometer*.

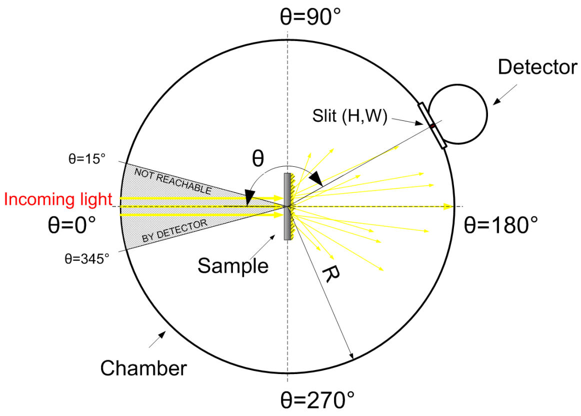

Figure 2.8: Schematic cross section of ARTA chamber along the measuring plane.

The basic concept of ADF value determination is illustrated in Figure 2.9. ADFs are both wavelength and angle dependent, $ADF(\lambda, \phi)$. The ADFs for transmitted light (ADF_T) can be obtained with a full angular range between 90° and 270°, when the detector rotates in front of the sample. While the ADFs for reflected light (ADF_R) is obtained only in the range of 15° to 90° and 270° to 345°, when the detector rotates in a plane behind the sample surface. By rotating the detector, the intensities of scattered light at discrete directions with a step of $\Delta\theta = 1^\circ$ can be determined, each angle measuring at one or a series of discrete wavelengths with a maximum step of 10 nm. With ARTA the absorbance $\mathcal{A}$ is measured. The intensity of light can be determined using Equation 2.24:

$$I = I_0 \cdot 10^{-\mathcal{A}} \tag{2.24}$$

Where I_0 is the intensity of incident light. Before the measurements the system is calibrated as $\mathcal{A} = 0$ detected at $\theta = 180^\circ$, when no sample is present.

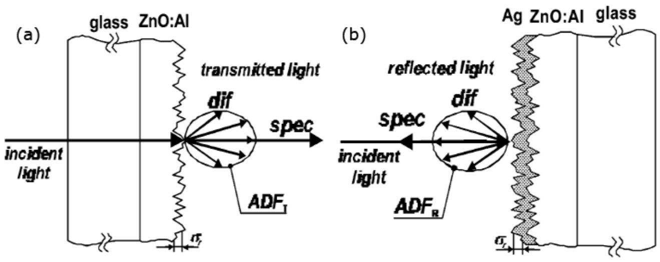

Figure 2.9: Determination of scattering parameters of a glass/AZO substrate in (a) transmission and (b) reflection [35].

These parameters used to be determined through Angular Resolved Scattering (ARS) setup, which can only measure at limited discrete wavelengths (usually with green or red laser). The new setup ARTA is capable of measuring a much broaden range of wavelength, normally from 220 nm to 2500 nm (limited by the fiber bundle and polarizer [36]). To test the reliability and accuracy of data obtained from ARTA, calibrations between these two setups was carried out at a single wavelength of 633 nm (red laser). One was through baseline calibration (with no sample), and the other two were commonly accepted standard samples: A Lambertian diffuser and an Asahi U-type TCO (from Asahi Glass Co.). Lambertian diffuser usually exhibits a standard cosine function of diffused light. Both measurements show good agreement with one another, if a normalization factor was applied to ARTA data with respect to ARS data, as shown in Figure 2.10. The result confirms the validity of measurement carried out with ARTA. Furthermore, less noise is observed from ARTA values than ARS. The angular interval of specular response without sample in ARS is $\Delta\theta \approx 4^{\circ}$, as described in reference [33]. While the *ADF*s of both baseline and Asahi show broader specular peak in ARTA. This is due to the broader incident beam in ARTA than the laser used in ARS, and also relative larger width of slit on the detector in ARTA which allows more light to come through.

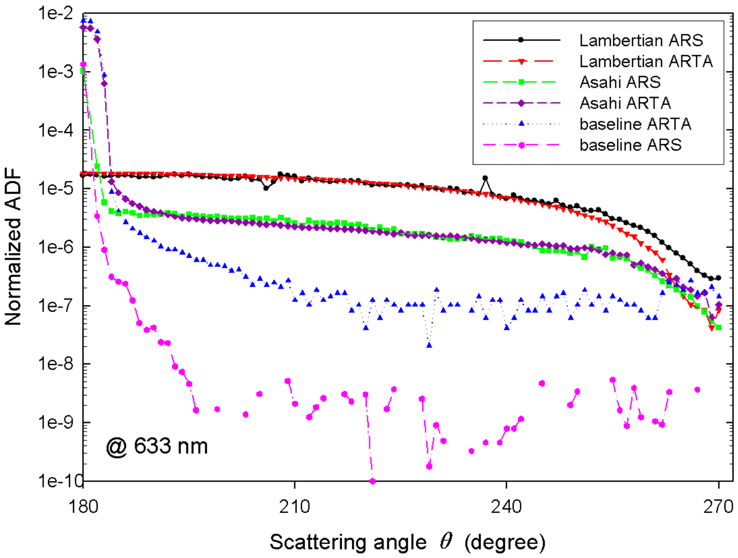

Figure 2.10: Baseline, Lambertian and Asahi *ADF* calibrations between old setup ARS and ARTA at 633 nm. The *ADF*s obtained from ARTA were normalized with respect to values from ARS. The normalization factor is 0.0075 for Lambertian and Asahi samples. The baseline from ARTA is multiplied with the same factor as for Lambertian and Asahi. Only angles between 180° and 270° are shown since the *ADF*s with these samples are symmetric with respect to $\theta = 180^{\circ}$.

2.3 Atomic Force Microscope (AFM)

Atomic Force Microscope (AFM) is a powerful tool to analyze the surface morphology. The morphological information is gathered by using a micro scale cantilever with a very sharp tip (probe) to scan up and down along the sample surface structure. When the probe is brought into proximity of a surface, forces between the probe and surface structure will lead to a deflection of the cantilever, and this deflection can be measured by using a laser spot reflected from the top surface of the cantilever into a photodiode.

In this study, an *NT-MDT®* *NTEGRA* AFM was used to obtain topographical pictures. AFM can be operated in several imaging modes, and we used non-contact mode. Additionally, the surface rms roughness can be determined and analyzed by specific user interface, for instance, *NT-MDT®* *Nova*. The surface rms roughness σ_{rms} is defined as:

$$\sigma_{\mathrm{rms}} = \sqrt{\frac{1}{N}\sum_{i=1}^{N}(z_i - \widehat{z})^2}, \tag{2.25}$$

where N is the number of data points, $\widehat{z}$ is the average surface level and z_i is the level of i-th point. Notice that σ_{rms} we used here only describes the surface structure along a vertical direction.

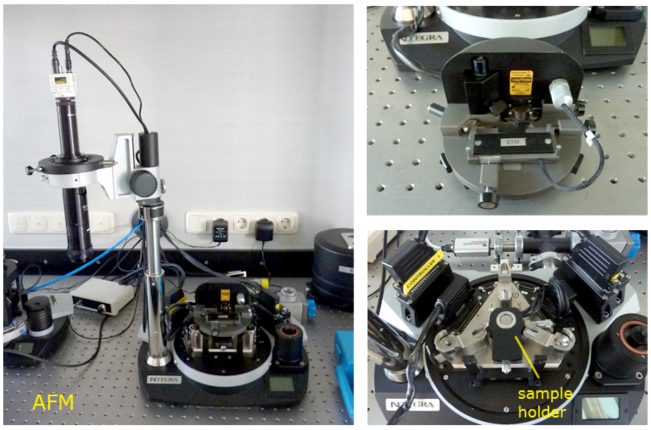

Figure 2.11: The photograph of Atomic Force Microscope (AFM) setup.

Chapter 3

Transparent conductive oxide films

In this Chapter, properties of TCO films are briefly discussed. We mainly focus on optical properties, aiming to gain a better understanding of scattering behaviors of different surface structure presented on TCO films. Surface morphology will be given in terms of pictures obtained from AFM. The TCO samples used in this study, fluorine doped tin oxide (SnO_2 or FTO), aluminum doped zinc oxide (ZnO:Al or AZO) and boron doped zinc oxide (ZnO:B or BZO), will be introduced at the end of each subsection.

3.1 Introduction of TCO films

Transparent conductive thin films of some metallic oxides, such as cadmium oxide, have been reported over a century's time [37]. They have been used for various applications such as transparent electrodes for flat panel displays, low emissivity windows or light emitting diodes, as well as thin film photovoltaics. TCO films are essential for almost all types of solar cells. Usually they are adopted with rough or textured surface or interfaces to gain sufficient light scattering. This effect was first described by Deckman et al.(1983) [38], due to the achievement of optical absorption enhancement in *a*-Si:H solar cell.

Generally, a good TCO layer usually meets several requirements as followed:

- Highly transparent in the entire photovoltaic active wavelength region. (Preferably transmission $> 85\%$)

- Suitable refractive index for coupling of light into the silicon absorber and minimizing reflections at the surface and between the interfaces. (Preferably approximately 2.3 for flat TCO and slightly higher for rough one, as $n_{\text{TCO}} = \sqrt{n_{\text{glass}} n_{a\text{-Si}}}$ in case of a glass/TCO/*a*-Si:H structure)

- Highly conductive to minimize the series resistance losses. (Preferably sheet resistance $< 10\ \Omega/\square$)
- Good ohmic contact with the *p*-layer for a *p*-*i*-*n* structure.
- Durable to hydrogen plasma during the silicon deposition process.
- Rough surface to longer the optical absorption path of light within the cell.

Owing to a well designed TCO layer, the effective optical absorption can be significantly increased while maintaining high photocurrents. In case of *a*-Si:H, the overall stability of the entire cell can be enhanced, and for μc-Si:H, a reduction of the deposition time can also be achieved [11].

Most of the TCOs are *n*-type semiconducting materials. Over years the most commonly used TCO has been indium tin oxide (ITO), or named tin doped indium oxide, which is a solid solution of tin oxide (SnO_2) and indium oxide (In_2O_3). This is mainly attributed to its superior electrical properties. However, the scarcity and high price of indium has driven ITO to be the most expensive TCO, thus cheap and non-toxic alternatives need to be found out. Recently, two promising candidates fluorine doped tin oxide (SnO_2:F) and aluminum doped zinc oxide (ZnO:Al) have been rapidly developed.

The most essential electrical property of TCO films is the conductivity of the charged carriers. In general, impurity doping results in an increase in carrier concentration and mobility [39], as a consequence a higher conductivity can be reached. However, from an optical point of view, increasing doping concentration will lead to higher free carrier absorption losses [16], which in turn decreases the transparency of the TCO layer. Therefore, high conductivity is usually achieved by high mobility, while keeping carrier density low.

For optical properties of TCO films the absorption coefficient α plays an important role. Generally α should be smaller than $10^4\ cm^{-1}$ in the near-UV and visible region. Both electrical and optical properties of TCO films can be strongly influenced by their thicknesses. A very thick TCO layer will lead to high absorption losses, while a very thin layer will enlarge the sheet resistance, thereby decrease the conductivity of the TCO layer. However, the conductivity can also be increased as the film becomes thick because thick films have low grain boundary scattering frequency [40]. An optimum to realize the overall performance always needs to be found.

Good TCO materials are always obtained through satisfying contradicting requirements. There is another additional requirement, the light trapping ability, i.e. the ability of light scattering at rough surface TCO films.

For a-Si:H and μc-Si:H solar cells, typical rms roughness of TCO layer is around 40-150 nm [16].

3.2 Fluorine doped tin oxide (FTO)

3.2.1 Properties

Tin oxide is a material that highly stable against acids and bases but rather unstable against hydrogen plasma [41]. It is usually made through sputtering [42, 43], chemical vapor deposition (CVD) [44], or spray pyrolysis [45–47]. Rough surface structure is developed during its deposition. When doping with F^- ions, the electron mobility can be markedly increased and resistivity is significantly reduced [46]. The sheet resistance of FTO decrease with increasing film thickness, whereas this decrease is very slow for thickness grater than approx. 0.5 µm [39]. The lowest sheet resistance was reported as 5.65 Ω/□ prepared by spray pyrolysis [48], and with the same sample an electron carrier concentration between 1.3×10^{20} and 13.2×10^{20} cm^{-3} was obtained. The bandgap of FTO is estimated to be between 3.6 and 4.4 eV [49, 50], depending on dopant concentration.

3.2.2 Experimental

The FTO substrates Asahi U-type substrates we used in this study were obtained from Asahi Glass Co, Ltd. Asahi has a random and pyramidal surface structure, as shown in AFM Figure 3.1. The rms roughness of Asahi is approximately 40 nm, which is determined by AFM. The thickness of Asahi is around 1 µm, with a sheet resistance of around 12.5 Ω/□ [51].

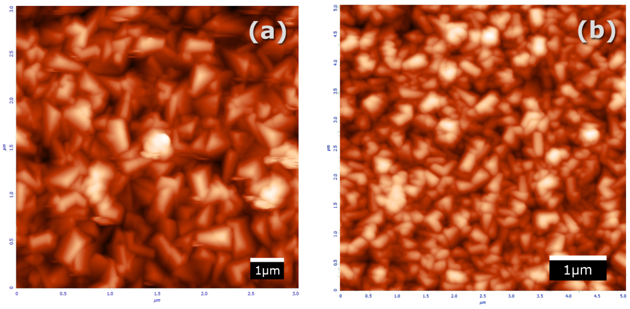

Figure 3.1: AFM micrographs of surface morphologies of Asahi U-type substrate, in (a) 3×3 µm^2 scale and (b) 5×5 µm^2 scale.

The IS measurements were carried out for Asahi samples at normal incidence. Wavelength ranges between 250 and 2500 nm with a step of 5 nm. For both transmittance and reflectance measurements, the integration time of detection was set as 1 second per wavelength for UV/Vis region and 4 seconds for NIR region in order to reduce noise. The VAS measurements were taken at both normal and oblique incidence, i.e. 0°, 30°, 45° and 60°, with a normal slit width of 1.6 mm. Usually wavelength between 300-800 nm was covered with a step of 10 nm. Angle range from 15° and 345° with an interval of 1° was used. Results of haze parameters and angular distribution functions for Asahi will be discussed in Chapter 4 Section 4.1.1.1 and 4.1.2.1. In order to better understand ARTA, we also investigated the influence of slit width on ADFs using Asahi. A full range (250-2500 nm) VAS measurement was also performed for Asahi with a slit width of 6 mm. Result of this part will be given in Appendix A.2.

3.3 Aluminum doped zinc oxide (AZO)

3.3.1 Properties

Zinc oxide is an abundant and low cost material. In contract with tin oxide it is little affected by hydrogen plasma but quite unstable in acids [41]. Therefore, the textured structure is generally achieved by etching with acid after the deposition. Usually ZnO is prepared by CVD [40, 52], or spray pyrolysis [53]. After deposition ZnO films have almost flat surface ($\sigma_{\mathrm{rms}} \approx$ 4 nm) [35]. They can be etched by dilute HCl, and a typical concentration of HCl is 0.5%. With different etching time, various surface structure in terms of different rms roughness can be obtained. This roughness can be later transferred to all internal interfaces within solar cell during deposition. Additionally, the etching process will reduce the thickness of ZnO films up to 400 nm for 30-second etching (initially δ = 700-900 nm) [54].

Pure zinc oxide has a high transparency in the visible region but poor conductivity. To avoid this disadvantage, ZnO films are usually obtained by doping with donor elements that substitute zinc atoms, such as aluminum, gallium or boron. The electrical conductivity of ZnO can be controlled over many orders of magnitude by doping with Al [16]. However, higher doping concentration leads to higher absorption, as already mentioned in Section 3.1. An example would be from reference [16] that, AZO with Al concentration only 1.6 wt% can arise strong absorption up to around 20% at NIR region. The bandgap of AZO is 3.3-3.5 eV [16,39].

3.3.2 Experimental

The AZO substrates we used were deposited using sputtering technique in DIMES, TU Delft. The surface structure is random and crater-like, with an increase of rms roughness from approximately 40 nm of 10-second etching to 100 nm of 40-second etching. A schematic diagram of surface structure is given in Figure 3.3, and AFM pictures with different etching time are shown in Figure 3.2. The initial thickness of AZO film is 2 µm, and is estimated to be around 1.5 μm after 40-second etching, which is still thicker than Asahi substrate. The estimated thickness and rms roughness of each sample is given in Section 3.5 Table 3.1.

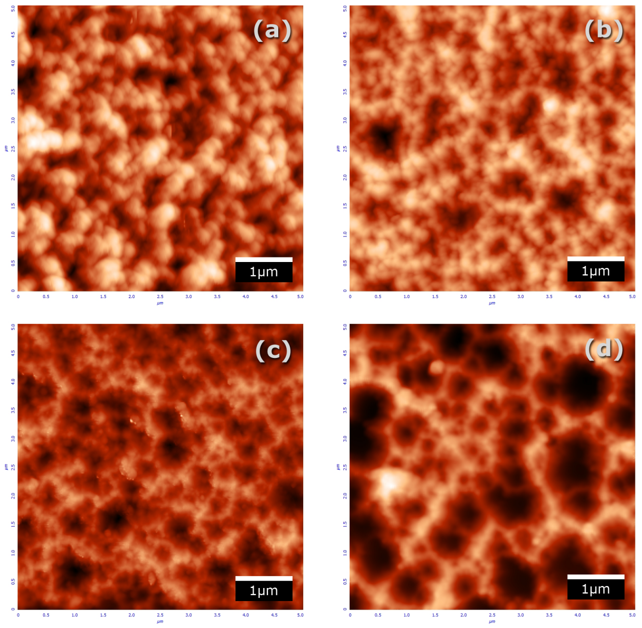

Figure 3.2: AFM micrographs of different surface morphologies of AZO, with (a) 10-second etching (b) 20-second etching (c) 30-second etching and (d) 40-second etching, in 5×5 μm^2 scale.

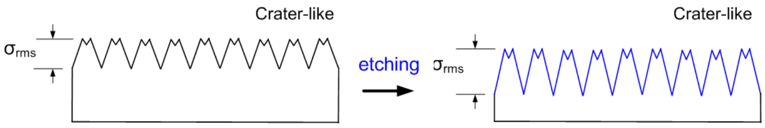

Figure 3.3: Schematic picture of ideal crater-like structure before and after etching.

To compare with Asahi, similar IS and VAS measurements were carried out for AZO substrates with different etching time. The influence on haze and ADFs with various rms roughness were investigated. A VAS measurement at oblique incident angles was performed using AZO 40-second. Results of haze and ADFs will be shown in Chapter 4 Section 4.1.1.2 and 4.1.2.2. Apart from understanding the performance of ARTA when changing the slit width, we also investigated the influence of integration time or PbS gain. Sample AZO 40-second was used to carry out these measurements, and results will be given in Appendix A.2.

3.4 Boron doped zinc oxide (BZO)

3.4.1 Properties

Boron doped zinc oxide is usually deposited through CVD or spray pyrolysis with diborane (B_2H_6) as a dopant gas. When Zn^{2+} ions are replaced by B^{3+} ions, the free electron density can be increased [52]. BZO with a sheet resistance of 10 Ω/□ and a thickness of 3 µm that has an electron density of 1.1×10^{20} cm^{-3} was reported by Wenas et.al [55]. Additionally, Hu and Gordon [40] reported a 483-nm film doping with 0.012 % B_2H_6 had a sheet resistance of 12.8 Ω/□, and IR reflectance close to 90 %. The bandgap of BZO varies from 3.3 to 3.7 eV [40, 53]. The refractive index of undoped ZnO films is around 1.95 and that of boron doped films is between 1.37 and 1.9 [40, 53].

3.4.2 Experimental

The BZO substrates used in our study are deposited by low pressure CVD (LPCVD), from PV-LAB, Ecode Polytechnique Fédérale de Lausanne, Neuchâtel (used to be IMT Neuchâtel before Jan 2009). In recent years, they presented a novel surface treatment that renders the surface morphology of LPCVD ZnO fully adapted to subsequent growth of μc-Si:H solar cells [56, 57]. The samples we used include two TCO substrates (type A and type B) without plasma treatment, and a group of type C substrates which are plasma treated for 0 minute (as a reference), 10 minutes, 20 minutes and 60 minutes. Type A has a carrier concentration of 1.4×10^{20} cm^{-3}, while type B and C have a lower concentration of 4×10^{20} cm^{-3}. The LPCVD-made substrate has a pyramidal surface structure. The surface will be slightly smoothened with a decrease of roughness from approximately 230 nm without treatment to 150 nm after surface treatment of 60 minutes. To differ from the surface after treatment, the pyramidal structure is considered as a V-type valley structure, while the one after treatment is called U-typed, as schematically illustrated in Figure 3.4. The thickness and rms roughness of each sample are given in Section 3.5 Table 3.1.

Figure 3.4: Schematic picture of ideal structure before and after plasma treatment.

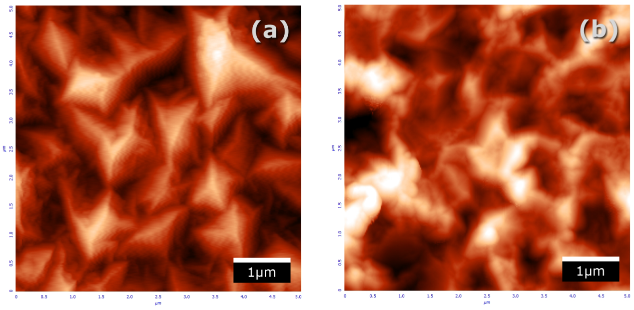

Figure 3.5: AFM micrographs of different surface morphologies of BZO, with (a) no treatment (b) 60-minute treatment, in 5×5 μm^2 scale. The shape of valley on the surface changes from V-type to U-type.

Similarly, BZO substrates were investigated through carrying out IS and VAS measurements. The results of haze parameters and ADFs will be discussed separately for BZO with or without plasma treatment. The influence of different treatment time was also investigated. Results will be discussed in Chapter 4 Section 4.1.1.3 and 4.1.2.3.

3.5 Summary of sample descriptions

To have a better view of these samples, some important features were summarized in Table 3.1, including the surface structure, rms roughness (σ_{rms}), layer thickness (δ) and bandgap (E_{g}).

Table 3.1: Description of samples

Sample		Surface structure	σ_{rms} (nm)	δ (μm)	E_{g} (eV)
FTO		random, pyramidal	~40	1	3.6-4.4 [49,50]
AZO	10"	random, crater-like	~40	2	3.3-3.5 [16,39]
	20"		~50	↓	
	30"		~60	↓	
	40"		~100	~1.5	
BZO	A	V-shape (pyramidal)	70	1.9	3.3-3.7 [40,53]
	B	V-shape (pyramidal)	150	4.8	
	C 0’	V-shape (pyramidal)	~230	~4.8	
	C 10’	↓	~190	~4.8	
	C 20’	↓	~170	~4.8	
	C 60’	U-shape	~150	~4.8	

Chapter 4

Scattering properties of transparent conductive oxide films

In this Chapter we present the results of scattering properties for the TCO films we introduced in Chapter 3. First the correlation among transmittance, reflectance and absorptance will be discussed through two representative TCO samples. Then, the descriptive parameters in terms of haze and angular distribution functions for both transmittance and reflectance will be explored and will be compared among one TCO sample to another.

4.1 Measurements with IS

4.1.1 Total/diffuse transmittance, reflectance and absorptance

When a TCO film is illuminated with a parallel beam of monochromatic light, the photons with lower energy than the bandgap of the TCO material will be absorbed by the layer, while higher energy photons will either transmit through or be reflected at the surface. The higher bandgap of TCO allows more shorter wavelength light to pass through, as the value of wavelength can be calculated via $\lambda = hc \ / \ E_{\mathrm{g}}$ (where h is Planck's constant and c is light velocity in vacuum). The transmittance, reflectance and absorptance spectra of both Asahi U-type and 40-second etched AZO substrates were plotted as a function of wavelength in Figure 4.1. The absorption was calculated using Equation 2.6. Both substrates exhibited high transmittance (approx. 80%) in the visable region. The transmission dropped very sharply in the UV region is due to the limitation of bandgap. Since FTO has a higher bandgap (3.6-4.4 eV) than AZO (3.3-3.5 eV), a narrowed absorption range in the UV region was observed for Asahi.

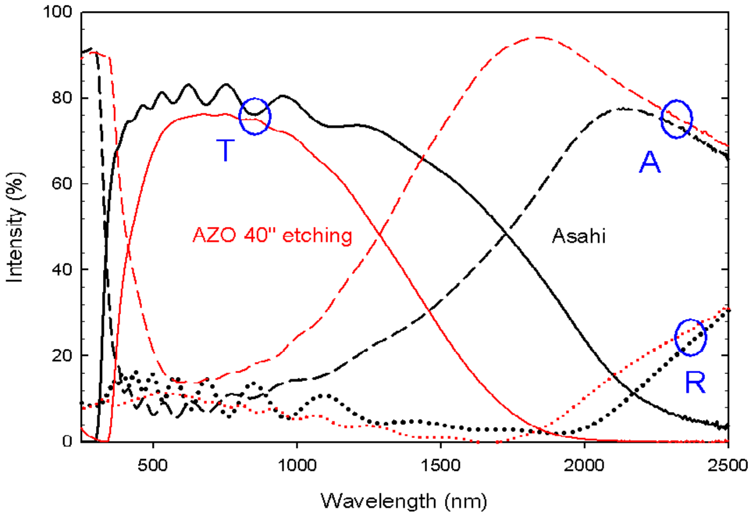

Figure 4.1: Total transmittance (T, solid), reflectance (R, dashed) and absorptance (A, dotted) of two substrates: Asahi (FTO, black) and ZnO:Al 40-second HCl etching (AZO, red).

Generally doped TCOs behave like metals in the IR region, having high reflectance. In the visible region, they behave like dielectrics and are highly transparent. The transition between these two behaviors is at the *plasma wavelength*. In Figure 4.1, FTO shows a higher transparency in the range 1000-2000 nm than AZO. This can depend on various parameters, such as growth conditions, thickness, doping concentration (or free carrier concentration), etc [39]. At longer wavelengths, the edge of reflectance is limited by the free carrier concentration. The higher the value of free carrier concentration, the shorter is the plasma wavelength. Figure 4.1 shows a red-shift transmittance for Asahi, this may be due to the less free carrier concentration in Asahi than in AZO.

4.1.1.1 Fluorine doped tin oxide (FTO)

The transmittance and reflectance result of FTO (Asahi U-type) is more specifically shown in Figure 4.2. Asahi shows a high transmittance and a low reflectance over the whole visible and NIR region. However, since the rms roughness is around 40 nm, the diffuse components are quite low and almost vanished at the wavelength of 1000 nm. Since Asahi U-type is a widely used commercial TCO substrate, in the following sections, we will present the results in comparison with Asahi.

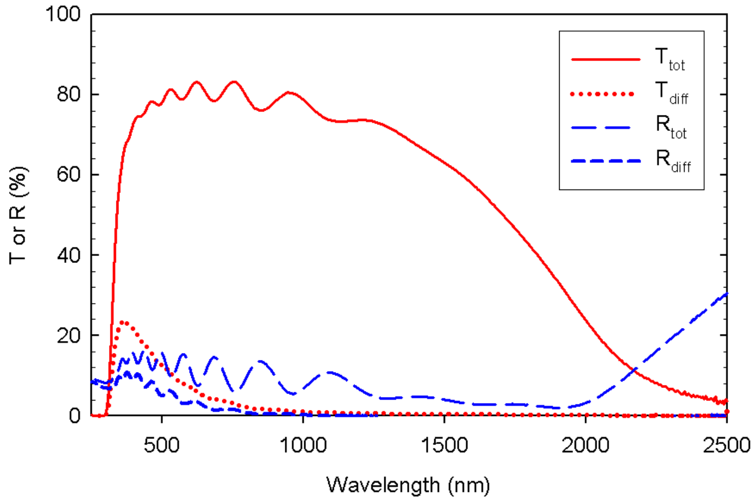

Figure 4.2: Total and diffuse transmittance (T_{tot} or T_{diff}) and reflectance (R_{tot} or R_{diff}) of Asahi.

4.1.1.2 Aluminum doped zinc oxide (AZO)

Figure 4.3 (a) illustrates the total and diffuse transmittance spectra of AZO substrates with different rms roughness. The diffuse transmittance increases significantly as the rms roughness becomes larger, while the total transmittance does not vary obviously. A slight red shift of total transmittance in the IR region is observed with relative rougher surfaces. Another observation is that the interference fringes are diminishing (for transmittance) or slightly flattened (for reflectance) with larger rms roughness surface. This is because the rough structure destroys the coherence of light. The fringes are more pronounced in reflection spectra, as shown in Figure 4.3 (b), this is because of the higher sensitivity of reflectance to the surface rms roughness than that of transmittance [58].

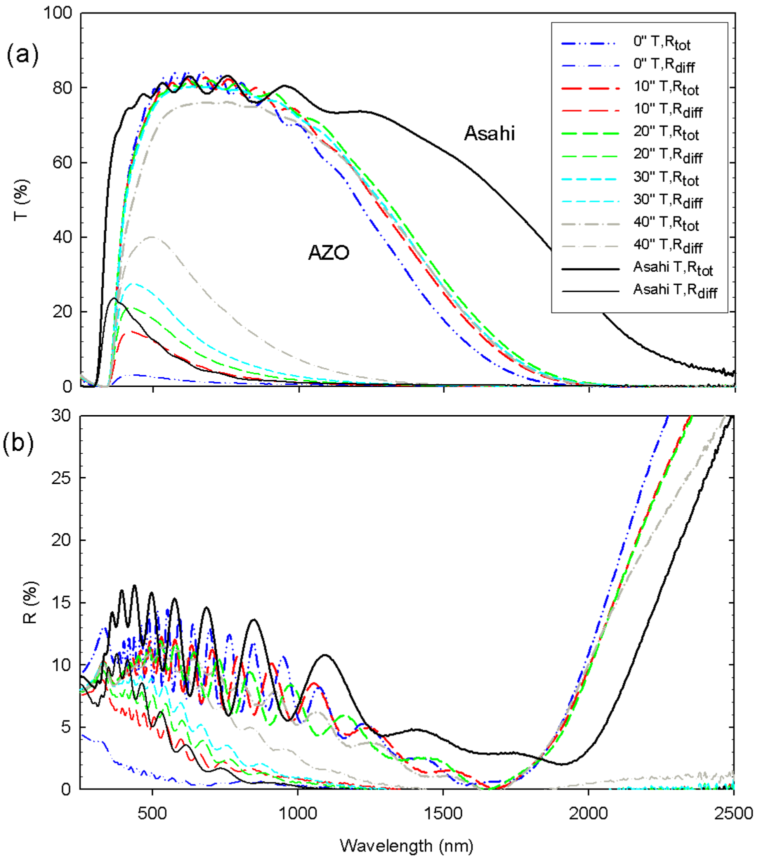

Figure 4.3: Total (thick line) and diffuse (thin line) (a) transmittance (T_{tot} or T_{diff}) and (b) reflectance (R_{tot} or R_{diff}) of AZO substrates with different etching time, ranges from 0 second (no etching) to 40 seconds. The spectra of Asahi are also involved for comparison.

4.1.1.3 Boron doped zinc oxide (BZO)

Similar measurements were carried out for BZO samples type A and B, and results were obtained in Figure 4.4. Figure 4.4 (a) shows that the total transmittance of type A and B were almost maintained at a level of 80% over the whole visible and NIR region. Type B shows a better transparency and broader wavelength edge than type A, due to a lower carrier concentration in type B than A. Higher reflectance is also found for BZO, especially type B, in Figure 4.4 (b). A large fraction of the visible light is diffused in both transmittance and reflectance. This is more obvious for type B, since type B has a rms roughness of around 150 nm, which is twice as large as type A, and four times larger than Asahi.

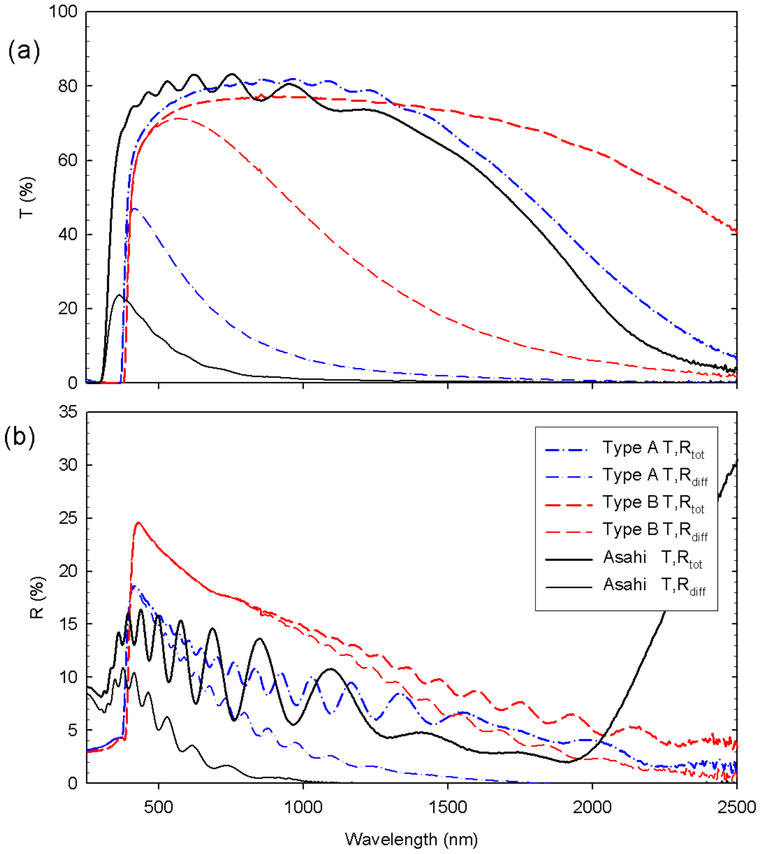

Figure 4.4: Total (thick line) and diffuse (thin line) (a) transmittance (T_{tot} or T_{diff}) and (b) reflectance (R_{tot} or R_{diff}) of two BZO substrates type A and B. The surface rms roughness of type A and B are approximately 70nm and 150nm, respectively. The spectra of Asahi are also involved for comparison.

The results of type C, a series of BZO samples with different time of plasma treatment, are shown in Figure 4.5. Similar trends are observed as untreated BZO samples. In Figure 4.5 (a), all these BZOs show broad transparency in the entire wavelength range of interest. T_{tot} shows an increased trend towards longer treated BZOs, and is more pronounced in visible region. The total amount of diffuse component is decreasing as the treatment time becomes longer, because from V-shape to U-shape the surface structure is smoothened which leads to a smaller rms roughness. A decrease in T_{diff} is observed in the NIR region for longer treatment time, while in the visible region, T_{diff} slightly increases and the peak of T_{diff} shifts to shorter wavelength. This indicates that shorter wavelength light is more preferable to be scattered at an U-shaped structure than V-shaped structure. For reflectance in Figure 4.5 (b), almost all the visible light is diffused by BZOs except the one treated for 60 minutes. Both transmittance and reflectance of BZO 60-minute show strong interference at longer wavelength region.

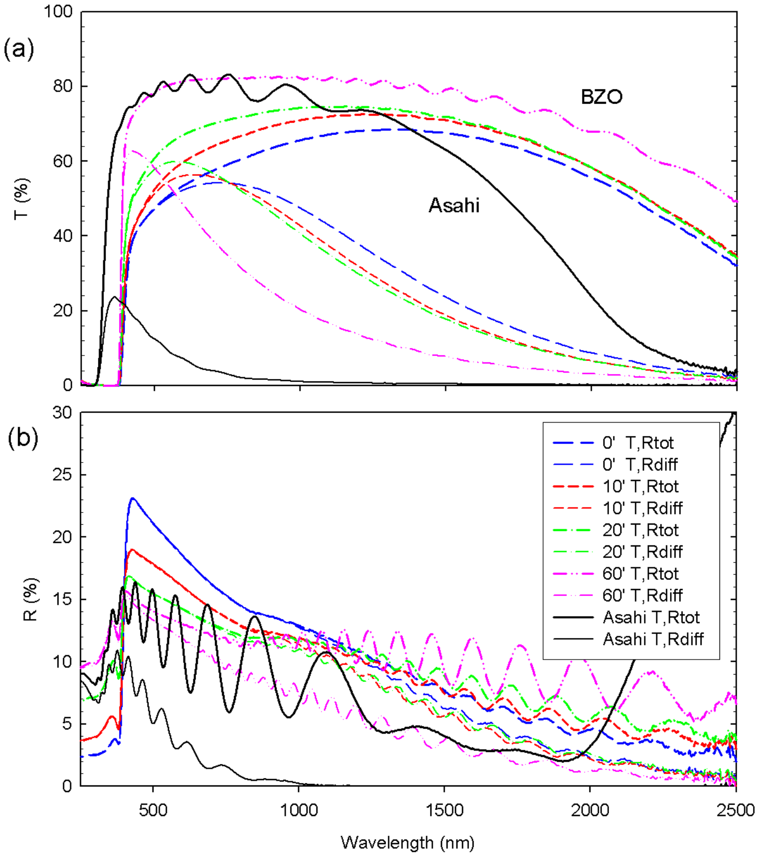

Figure 4.5: Total (thick line) and diffuse (thin line) (a) transmittance (T_{tot} or T_{diff}) and (b) reflectance (R_{tot} or R_{diff}) of several BZO substrates with different plasma treatment time, ranges from 0 minute (no treatment) to 60 minutes. The shape of valleys on the surface changes from V-type gradually to U-type, as the treatment time becomes longer. The spectra of Asahi are also involved for comparison.

4.1.1.4 Comparison between two BZO samples with similar rms roughness

Since BZO type B (without plasma treatment) and BZO with 60-minute treatment have similar rms roughness (approx. 150 nm), it is interesting to compare these two in terms of their T_{tot}, T_{diff}), R_{tot} and R_{diff}) in the same graph. Figure 4.6 presents the difference between them. With similar rms roughness, BZO without plasma treatment obtains a slight lower T_{tot} but very high T_{diff} compared with BZO 60-minute. From this we conclude that the rms roughness is not sufficient to precisely describe the scattering behavior of TCOs, other features such as lateral morphology is needed as well.

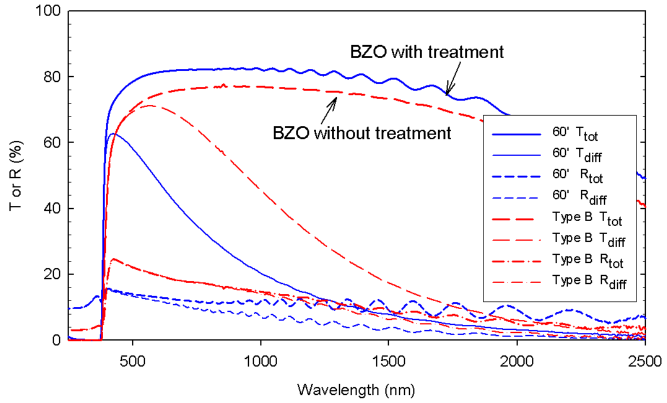

Figure 4.6: Comparison of T_{tot}, T_{diff}, R_{tot} and R_{diff} between BZO type B (red) and BZO 60-minute plasma treatment (blue).

4.1.2 Haze for transmission and reflection

4.1.2.1 Fluorine doped tin oxide (FTO)

Haze, which is defined as diffuse component divided by total, can be considered as the ability of light scattering that independent of total transmission or reflection. The haze parameters H_T and H_R of Asahi are shown in Figure 4.7. Both H_T and H_R show decreasing trend as wavelength becomes larger because shorter wavelength light scatters more efficiently. A higher H_R than H_T is observed for almost all samples, which can be explained as the scattering in reflection is more obvious than in transmission [54].

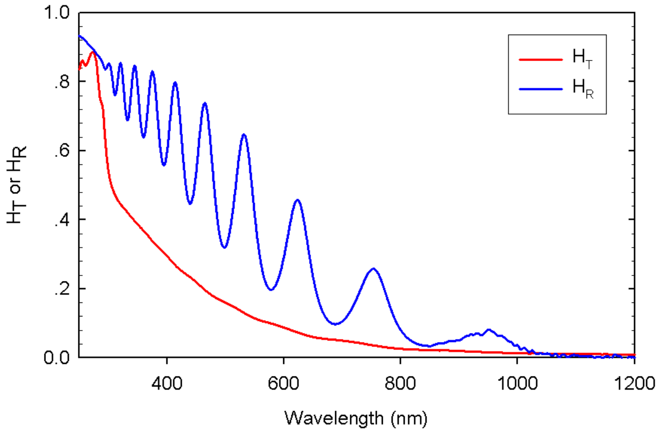

Figure 4.7: Haze for transmittance (H_T) and reflectance (H_R) of Asahi.

4.1.2.2 Aluminum doped zinc oxide (AZO)

The haze H_T and H_R with various time scale etched AZO substrates are plotted as a function of wavelength in Figure 4.8. We are interested only in wavelength between 400 nm and 1800 nm as for AZO there is almost no light transmission upon wavelength larger than 1800 nm (see Figure 4.1). Both H_T and H_R decrease as wavelength becomes larger, which again shows that light with longer wavelength suffers less scattering. This is due to the wavelength of light becomes more comparable with the dimension of rms roughness.

As indicated in Figure 4.8, the H_T is enhanced as etching time becomes longer which means a larger rms roughness. Figure 4.8 (a) shows that the H_T of Asahi almost matches with AZO 10-second with wavelength larger than 400 nm, as they have a similar rms roughness of around 40 nm.

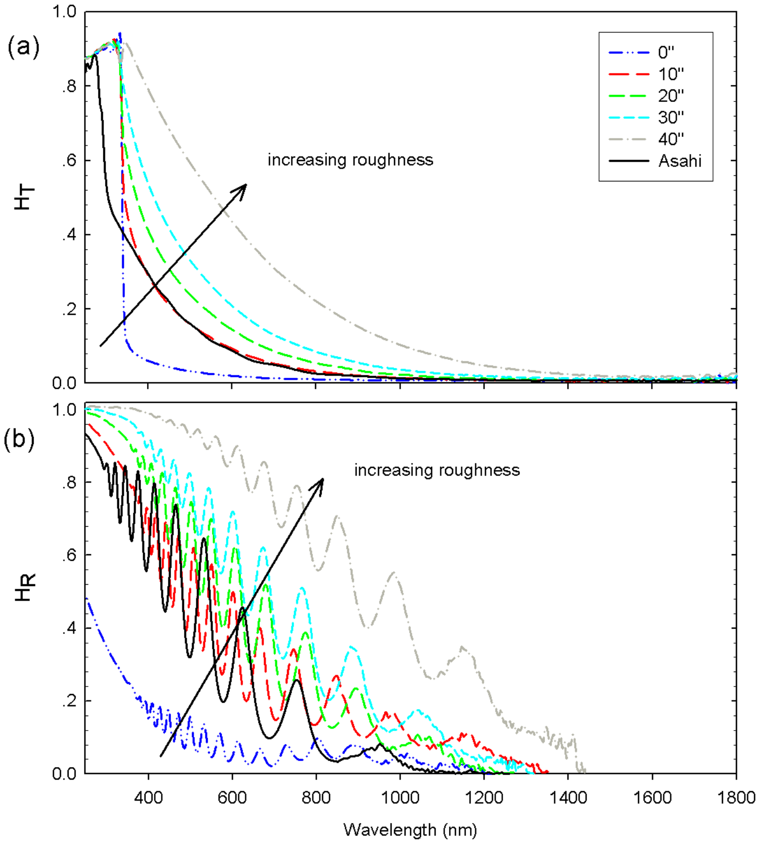

Figure 4.8: Haze for (a) transmittance (H_T) and (b) reflectance (H_R) of AZO substrates with different etching time, ranges from 0 second (no etching) to 40 seconds. The spectra of Asahi is also involved for comparison.

4.1.2.3 Boron doped zinc oxide (BZO)

A decreasing trend with longer wavelength can also be found for BZO samples type A and B in Figure 4.9. Light scattering is substantially enhanced towards longer wavelengths with increasing rms roughness. For type B, more than 90% of the visible light is scattered either in transmission or reflection. This indicates that rms roughness of around 150 nm with a pyramidal (V-shaped) surface is quite favourable in visible light scattering. Additionally, the effect that light scattering is more pronounced in reflection than transmission can also be seen with BZO samples.

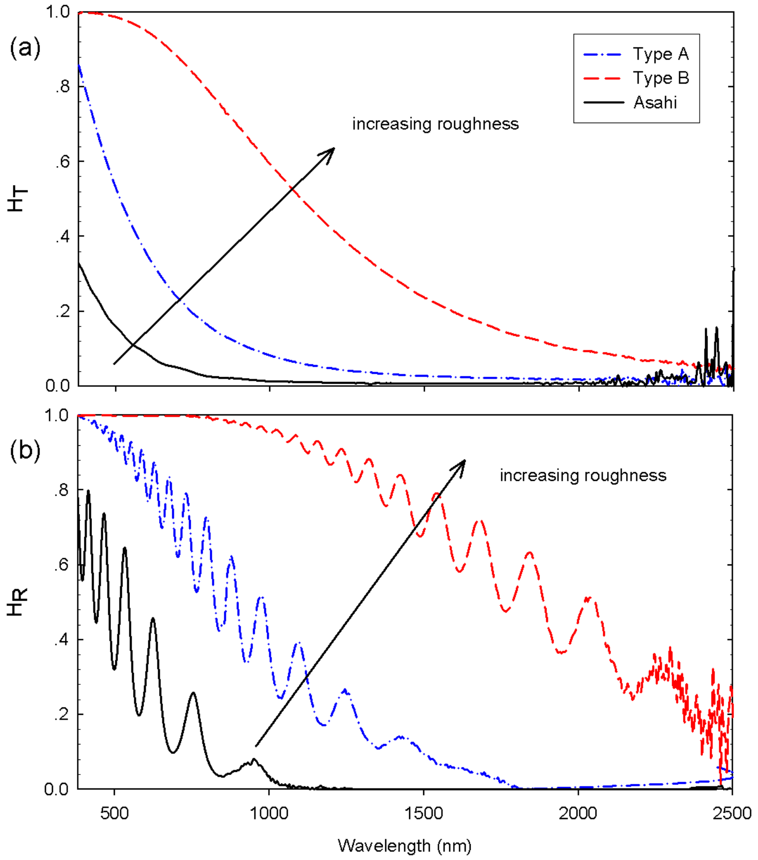

Figure 4.9: Haze for (a) transmittance (H_T) and (b) reflectance (H_R) of type A and type B BZO substrates with rms roughness of 70nm and 150nm, respectively. The spectra of Asahi is also involved for comparison.

The main difference between BZO type C samples and type A or type B is the plasma treatment. The shape of valley on sample surface gradually turns from V-type to U-type as the treatment time becomes longer (see AFM Figure 3.5), and the rms roughness decreases slightly (schematically shown in Figure 3.4). As a result, both H_T and H_R shrink towards shorter wavelength, and more obviously in BZO 60-minute. However, a decrease in rms roughness, hence a reduction of haze value, does not mean that the performance of the entire cell will be negatively influenced. Although BZO 60-minute has a lower light scattering ability than untreated BZOs, the relative smoother and curved structure of BZO 60-minute can dramatically improve the electrical performance of the entire cell [57]. The reason is that the removing of tips (from V-shape to U-shape) on the TCO surface will lead to less cracks in the *i*-layer during deposition. In that case, a higher quality of absorber and enhancement of light utilization can be achieved.

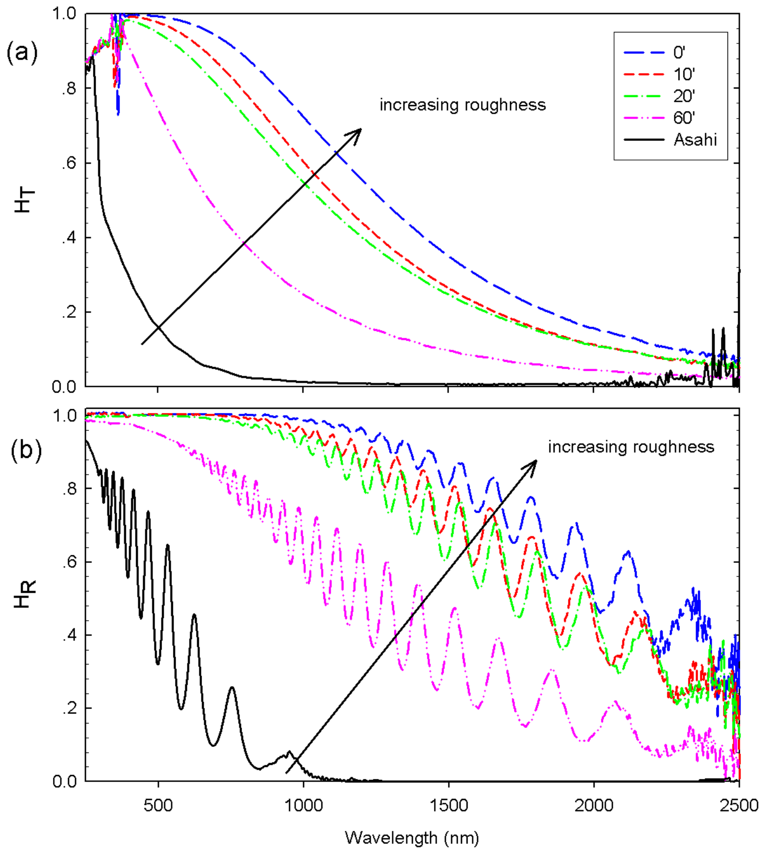

Figure 4.10: Haze for (a) transmittance (H_T) and (b) reflectance (H_R) of several BZO substrates with different plasma treatment time varies from 0 minute (no treatment) to 60 minutes. The shape of valleys on the surface changes from V-type gradually to U-type, as the treatment time becomes longer. The spectra of Asahi is also involved for comparison.

4.1.2.4 Comparison between two BZO samples with similar rms roughness

We compare haze parameters of samples (BZO type B and BZO 60-minute) with similar rms roughness. The result is presented in Figure 4.11. We can see that light scattering ability of V-shaped BZO type B is much higher than U-shaped BZO 60-minute. This again indicates that rms roughness is not the only parameter to determine light scattering behaviors of TCOs. As shown in Section 3.4.2 Figure 3.4, the lateral feature changes from V-type, pyramidal structure, to U-type, with smoothened tips and hollowed sides of those pyramids. Figure 4.11 shows that this change could exhibit significant difference in haze between similar rough samples.

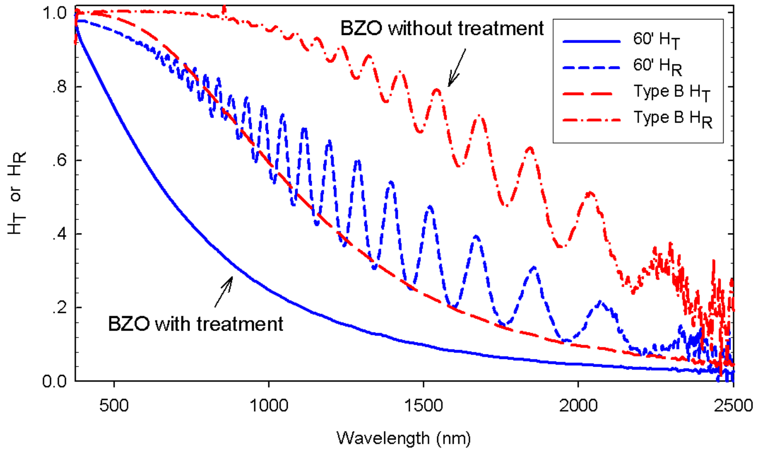

Figure 4.11: Comparison of H_T and H_R between BZO type B (red) and BZO 60-minute plasma treatment (blue) of which have similar rms roughnesses.

4.2 Measurements with ARTA

4.2.1 *ADF*s for transmission and reflection at normal incidence

4.2.1.1 Fluorine doped tin oxide (FTO)

In order to investigate the angular dependency of light scattering behaviors, we also measured the angular distribution functions (*ADF*s) for these three types of TCOs. Usually measurements were carried out between wavelength 300 nm and 1200 nm, using *p*-polarized light at normal incidence (measurements at oblique incidence will be explored in Section 4.2.2). Only wavelength ranges from 300 nm to 800 nm were plotted, since for higher wavelengths the signal-to-noise ratio became too low, and little features can be extracted from those spectra. Since ADF_R can not be measured in a full 180° range (angles between 0° and 15°, and between 345° and 360° can not reached by detector), we will mainly focus on ADF for transmittance.

The ADF_T and ADF_R for Asahi at six representative wavelengths are shown in Figure 4.12. Since the intensity for investigated sample is symmetric with respect to $\theta = 180^\circ$, only angles between 90° and 180° are present for ADF_T and from 15° to 90° for ADF_R. Significant noise occurs in the wavelength range between 800 nm and 900 nm as a consequence of both detector and lamp exchange, which becomes more pronounced when the light signal is small. The noise can be slightly smoothened through increasing the integration time of measuring system, and examples will be shown in the Appendix A.2.

The total amount of scattered light of transmission is much higher than reflection for Asahi, and both of them become weaker towards larger angles for all the wavelengths. With an increasing wavelength, we observed a decreasing intensity of scattered light and an increase in specular light. This is because light with shorter wavelength becomes more comparable with the dimension of surface structure hence is easier to be scattered [59]. A decreasing scattered light together with an increase of specular light as wavelength becomes larger leads to a decline of H_T in the visible region, and this is in agreement with the results described in Figure 4.8 (a). In this case the specular light intensity increases more rapidly than decrease of scattered component, leading to a steeper decline of H_T for Asahi. A three dimensional picture is shown in Figure 4.13 to have a better view of relationship between haze and ADFs as a function of wavelength.

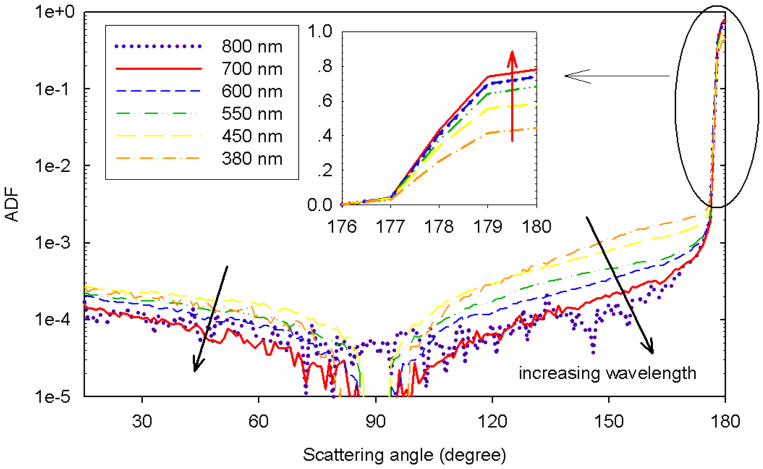

Figure 4.12: Angular distribution of transmitted (ADF_T) and reflected light (ADF_R) of Asahi substrate. A group of representative wavelengths in visible spectrum region are selected for comparison. An enlarged picture on specular transmittance in linear scale is also involved.

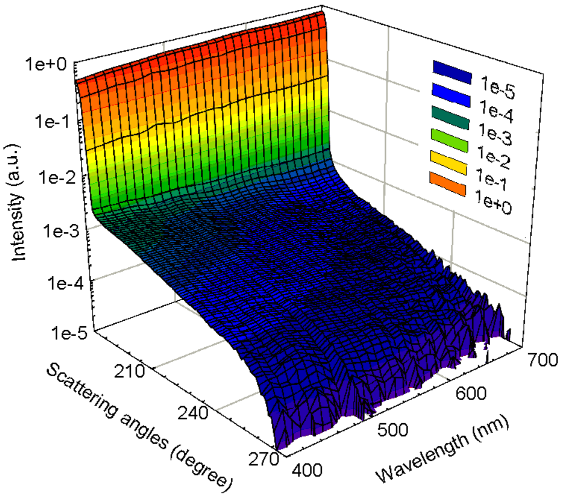

Figure 4.13: Three dimensional picture of *ADF*s in the visible region between 180° and 270° for Asahi substrate.

4.2.1.2 Aluminum doped zinc oxide (AZO)

Figure 4.14 shows *ADF*s for AZO in a way that different rough structures are compared at three representative wavelengths. A declining trend of the amount of scattered light towards shallow angles is also observed for AZO samples. At each subgraph, it can be seen that the light is scattered more with increasing rms roughness at all these wavelengths. Furthermore, the spectra in Figure 4.14 (800 nm) becomes less noisy with rougher samples since higher rms roughness structure can achieve stronger scattering so that the signal-to-noise ratio becomes relative higher. As described before, shorter wavelength light is more easily to be scattered. This behavior is also present at AZO samples, and can be clearly observed in Figure 4.14. In the subgraph (a) the 800-nm light can only be markably influenced when the etching time becomes 40 second, i.e. reaches a rms roughness of around 100 nm, while the 450-nm one is more sensitive to rms roughness changes and can be significantly scattered when the etching time reaches the level of 10 second, as shown in Figure 4.14 (c).

In addition, we also investigated the wavelength dependency of *ADF*s for AZO samples. Figure 4.15 presents the result with respect to etching time. Comparing Figures 4.15 (a) to (c) we observe that, with higher rms roughness, more light is scattered into smaller angles. This is in agreement with the results from a previous study [35]. Furthermore, the increase of scattered light intensity and consequently a reduction of specular light intensity with decreasing wavelength also found for all rms roughness samples. This again results in a downward trend of H_T as shown previously in Figure

4.8. Figure 4.15 (a) (no etching) shows that as wavelength becomes longer, the amount of decreased scattered light is smaller when compared to the increase of specular light intensity, this leads to a rapid drop of H_T in the visible region. In contrast with AZO 40-second, a stronger decrease in scattered light intensity than the increase of specular light intensity is found, which contributes to a gradual decline of H_T. These all match the results obtained from Figure 4.8.

The changes of ADFs in Figure 4.14 and 4.15 are also in agreement with reference [31], where the relationship between surface roughness and the intensity of specular reflectance was described. As we obtained from these graphs, when the surface rms roughness is constant, the specular component increases with longer wavelength, while diffuse component decreases, and with a fixed wavelength, the specular component declines as the rms roughness becomes larger, at the same time the diffuse component increases.

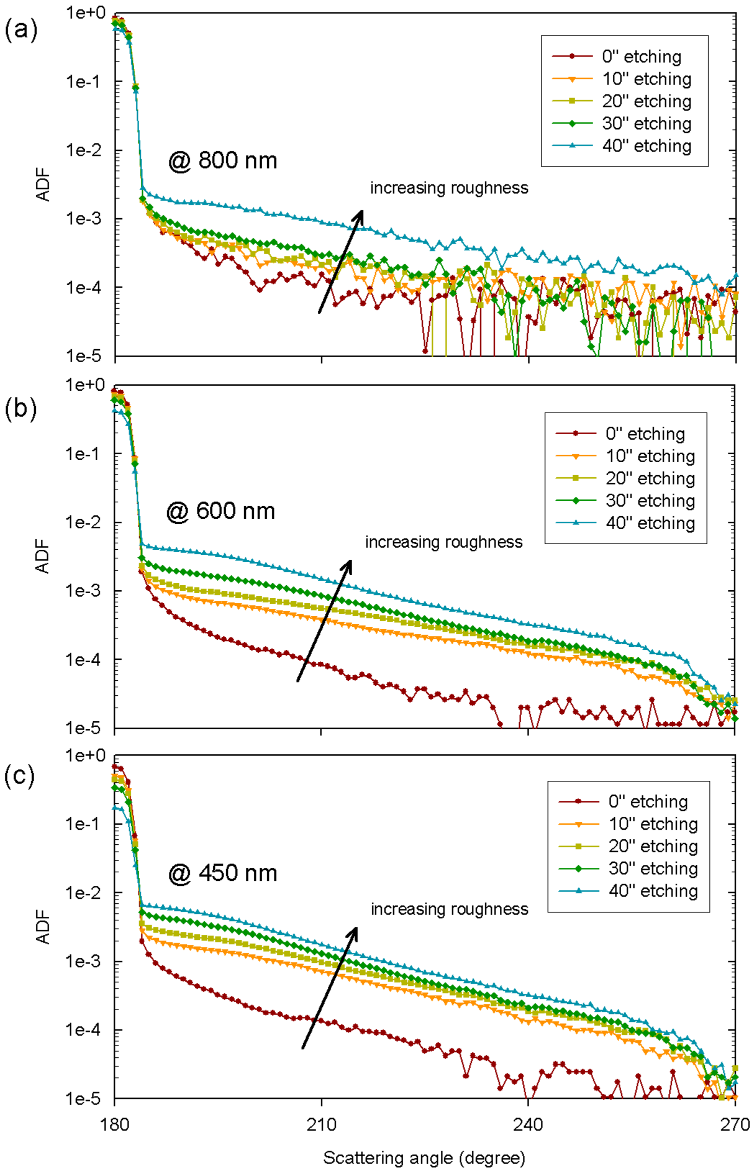

Figure 4.14: Angular distribution of transmitted light (ADF_T) of AZO substrates with different etching times ranges from 0 second (no etching) to 40 seconds. Three representative wavelengths (a) 800nm (b) 600nm and (c) 450nm are selected for comparison.

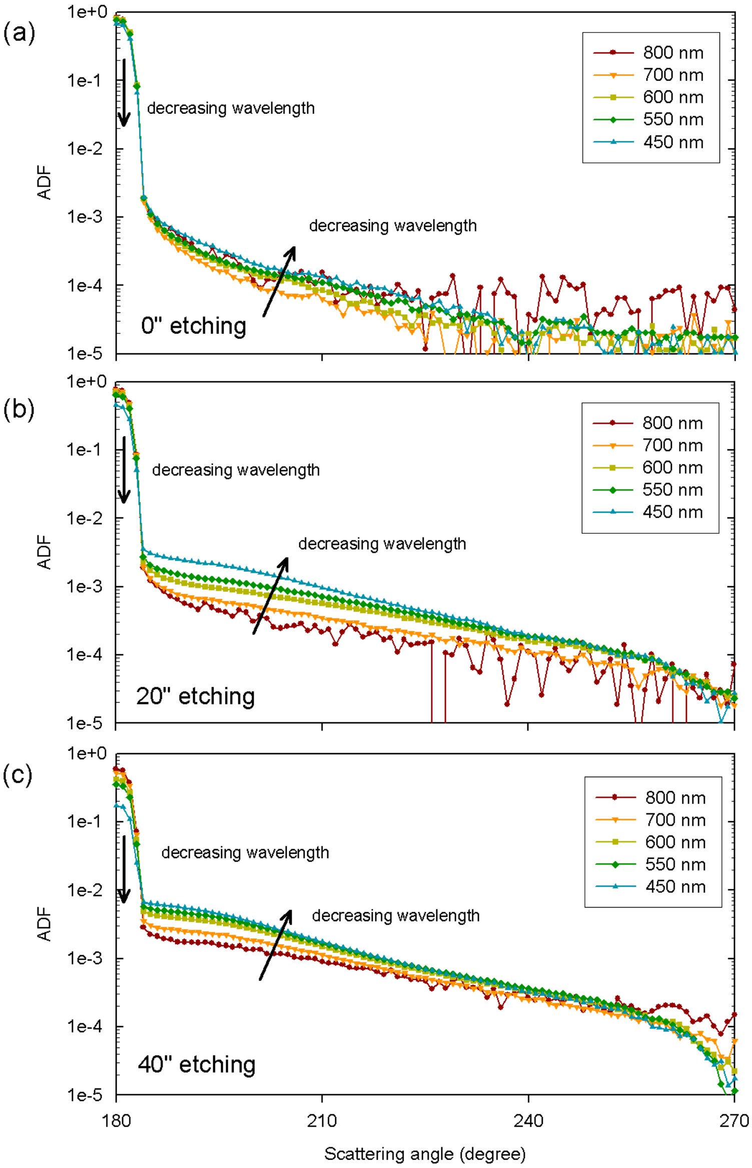

Figure 4.15: Angular distribution of transmitted light (ADF_T) of AZO substrates with different etching times ranges from 0 second (no etching) to 40 seconds. Three representative etching times (a) 0 second (b) 20 seconds and (c) 40 seconds are selected for comparison.

4.2.1.3 Boron doped zinc oxide (BZO)

BZO type A and type B, with a pyramidal surface structure and a rms roughness of around 70 nm and 150 nm, respectively, are expected to behave differently in ADF profiles in comparison than Asahi and AZO, that shows a crater-like structure. As can be seen in Figure 4.16, both type A and B substrates exhibit a very flat profile of scattered light intensity against angular changes. This indicates that light tends to be scattered uniformly in all directions. For Type A, the wavelength dependency can still be distinguished, and light with shorter wavelength is scattered more efficiently, similar as AZO and Asahi. For type B, a rather different behavior is observed. The intensity of scattered visible light becomes nearly independent of wavelength, particularly in the shallow angle range ($\theta > 210^{\circ}$). This may attribute to the high rms roughness of type B. All wavelengths in visible region seem to have comparable dimension to the structure. As a result, with a significant drop of specular light intensity with shorter wavelengths, H_T will decrease much slower. This is also in agreement with the haze profile of BZO type B shown in Figure 4.9. In particular at 450 nm, the specular component of BZO type B is almost vanished, which can be corresponded to $H_T \approx 1$ at this wavelength.

The influence of rms roughness on different wavelengths is also investigated for BZO type A and type B, as shown in Figure 4.17. The higher rms roughness leads to a much larger intensity of scattered light, which is more pronounced at longer wavelength. This is very similar as result from AZOs with different rms roughness described in Section 4.2.1.2. The discrepancy of the amount of scattered light becomes more severe as wavelength becomes longer, as can also be observed from H_T in Figure 4.9. The influence will becomes smaller with very long wavelength, since at that range even a rms roughness of 150 nm feature is not large enough to scatter light any more.

The ADF behaviors of BZO type C samples supplied with different time of plasma treatment are investigated. Figure 4.18 emphasizes the wavelength dependency on ADF_T at three representative treatment time. BZO type C with no treatment is similar sample as BZO type B, so that they perform quite similar in ADF_T. But subgraph (a) gives a more obvious trends showing that shorter wavelength light is scattered less in this structure. Furthermore, striking difference is found when the treatment time becomes longer, which means surface structure turns gradually from V-shaped into U-shaped. Light is strongly scattered towards smaller angles with longer time treated structures. The specular component increases dramatically which leads to a decrease of H_T as shown in Figure 4.10. For BZO 60-minute, the decrease of scattered light intensity is minor compared with the rise in specular light as wavelength becomes longer, so that a rather flat slope of H_T is observed in the visible region.

Figure 4.19 shows the influence of plasma treatment on light with different wavelength. Light scattering becomes stronger with an increasing rms roughness is only valid in the relative shallow angle region ($\theta > 210^{\circ}$). At smaller angle range, BZO 60-minute, which has a relative low rms roughness, exhibits a much higher intensity of scattered light and lower intensity of specular light, especially for shorter wavelength. From this we conclude that there is a large contribution of changing the scattering behaviors (angular distribution of scattered light) from the special U-shaped structure, and the rms roughness can only describe some structures, such as crater-like AZOs, but not all.

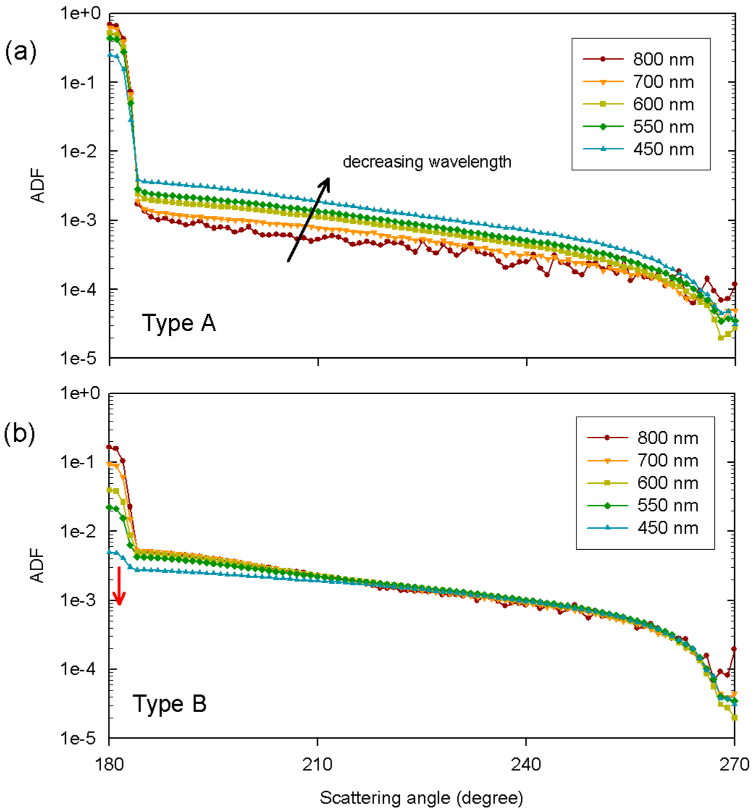

Figure 4.16: Angular distribution of transmitted light (ADF_T) of BZO substrates (a) type A and (b) type B, with a rms roughness of 70nm and 150nm, respectively.

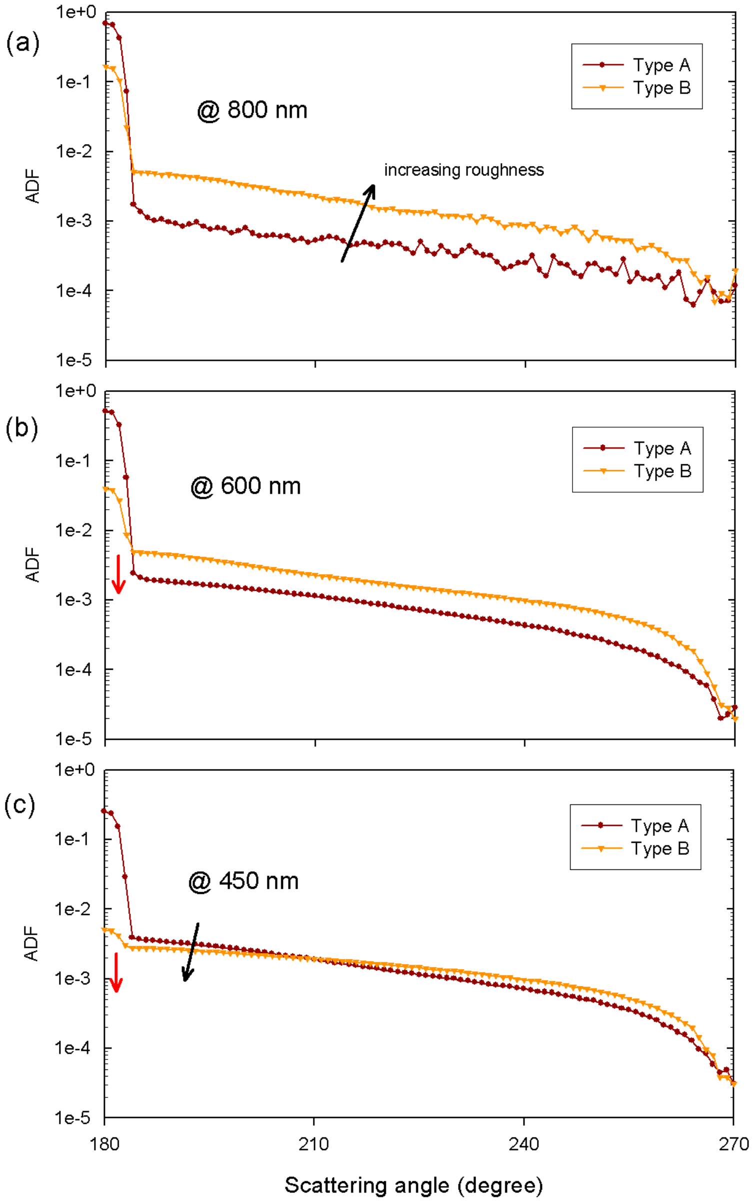

Figure 4.17: Angular distribution of transmitted light (ADF_T) of BZO substrates type A and B. Three representative wavelengths (a) 800nm (b) 600nm and (c) 450nm are selected for comparison.

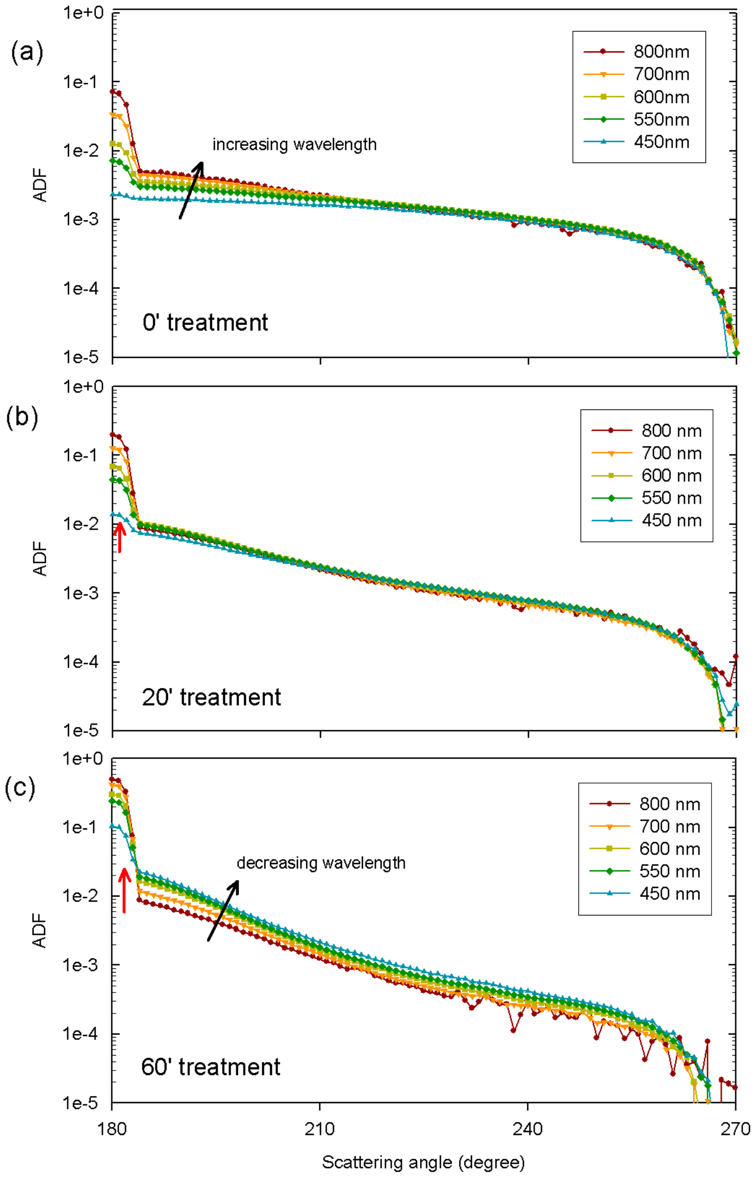

Figure 4.18: Angular distribution of transmitted light (ADF_T) of BZO substrates with plasma treatment times ranges from 0 minute (no treatment) to 60 minutes. Three representative treatment times (a) 0 minute (b) 20 minutes and (c) 60 minutes are selected for comparison.

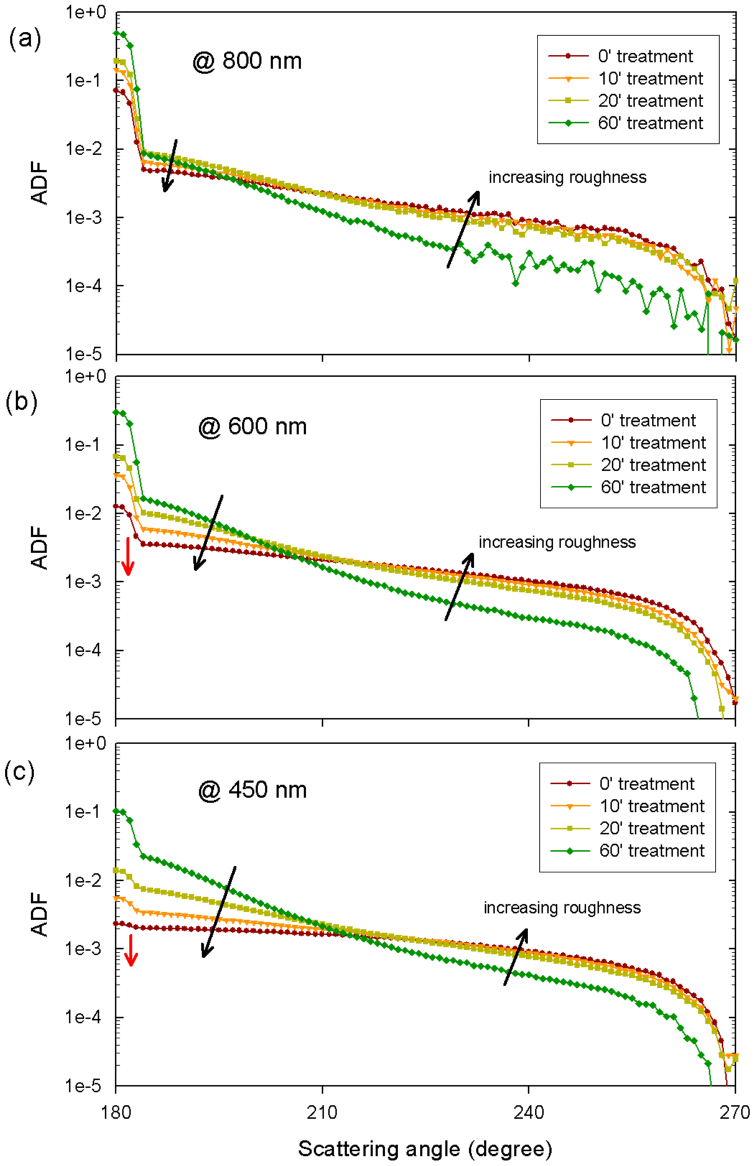

Figure 4.19: Angular distribution of transmitted light (ADF_T) of BZO substrates with different plasma treatment times ranges from 0 minute (no treatment) to 60 minutes. Three representative wavelengths (a) 800nm (b) 600nm and (c) 450nm are selected for comparison.

4.2.1.4 Comparison between FTO and AZO samples with similar rms roughness

As the total amount of scattered light is determined from haze value, it is interesting to compare the shapes of ADFs of different samples with similar haze profile (in this case even similar rms roughness of approx. 40 nm), to gain a better understanding upon how light scattering is distributed with different TCOs. In Figure 4.20 we plotted H_T and ADF_T (at 450 nm and 700 nm) between AZO 10-second etching and Asahi substrates. Difference in H_T is only observed in the shorter wavelength ($\lambda < 400$ nm) range. The 450-nm light tends to be scattered more in the smaller angle range for AZO 10-second while for Asahi shallow angles ($\theta > 210^{\circ}$) are more favorable with 450-nm light. This again proves that vertical structure description is not sufficient to explain the scattering behavior, in this case the small structures on AZO surface may have inclinations that are better in scattering light towards smaller angles. The difference of intensity of scattered light present at different angle range is compensated with each other, which leads to a similar H_T at 450 nm. The longer wavelength light suffers less scattering, so that the deviations due to structure difference between these two samples is small.

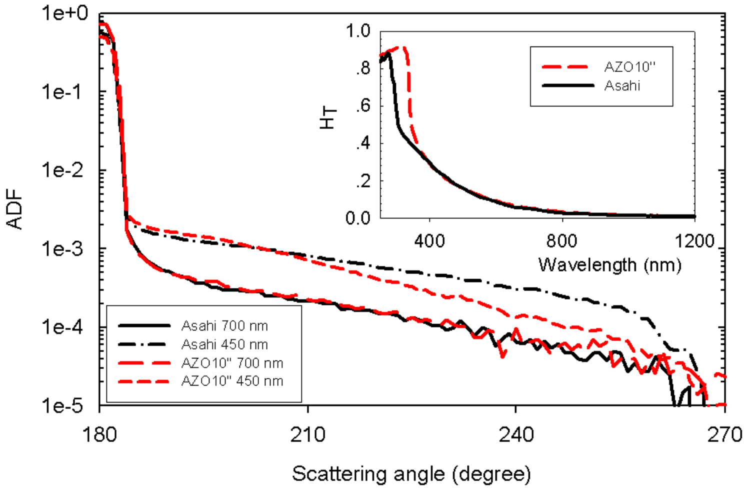

Figure 4.20: Comparison of ADF_T at two representative wavelengths between AZO 10-second (red) and Asahi (black) of which have similar H_T. The haze spectra is also embedded.

4.2.1.5 Comparison between AZO and BZO samples with similar haze

A comparison between BZO type A and AZO 40-second in terms of their ADF_T at two representative wavelengths is carried out in Figure 4.21, as these two samples show a very similar haze profile (in this case different rms roughness). The slight discrepancy between the two H_T occurs mainly in the visible region. A steeper slope of ADF is observed for AZO 40-second than BZO type A, which indicates that compared with BZO samples, which have pyramidal structure surfaces, AZO (crater-like structure) are more likely to scatter light into smaller angles ($\theta < 210^{\circ}$). This is in agreement with the result we obtained in Section 4.2.1.5, where the difference on ADF_T between crater-like (AZO 10-second) and pyramidal (Asahi) structures were discussed. Therefore we conclude that similar haze profile can exhibit quite different angular distributions of scattered light, and crater-like structures (AZO) are more favorable of smaller angle scattering while pyramidal structures (Asahi and BZO type A and B) scatter light in a broader range of directions in comparison with the former structure.

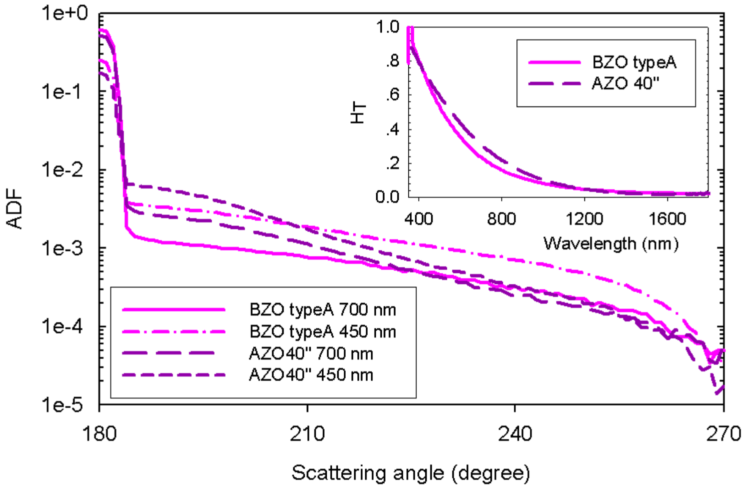

Figure 4.21: Comparison of ADF_T at two representative wavelengths between BZO type A (pink) and AZO 40-second (purple) of which have similar H_T. The haze spectra is also embedded.

4.2.2 ADFs for transmission and reflection at oblique incidence

The difference of ADFs for two TCO films with various incident angles were investigated in this section. The angle of 30°, 45° and 60° were chosen in the measurements, and the results in comparison with normal incidence were presented in Figure 4.22 for Asahi and Figure 4.24 for AZO 40-second etching.

4.2.2.1 Fluorine doped tin oxide

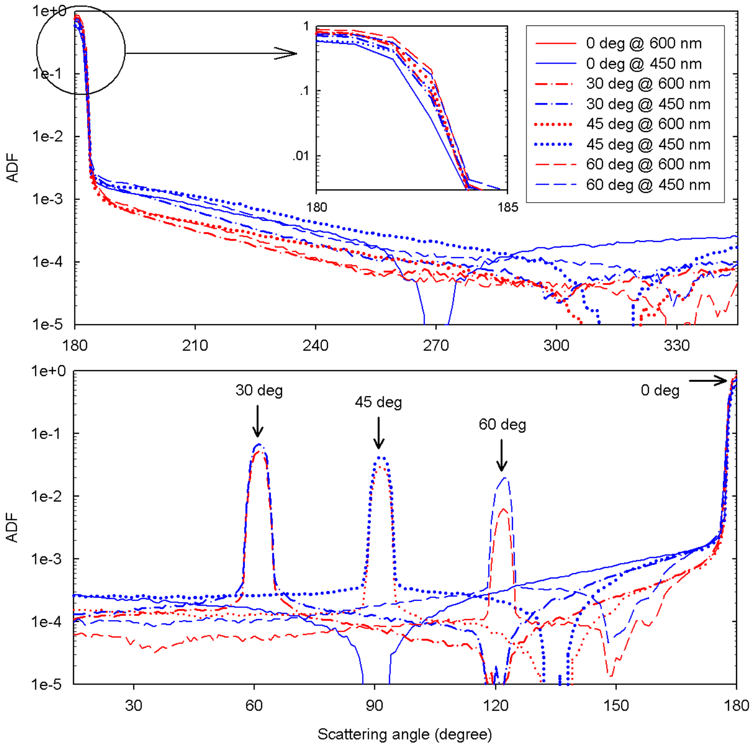

Figure 4.22: Angular distribution of transmitted (ADF_T) and reflected light (ADF_R) with different incident angles of light for Asahi substrate. Two representative wavelengths 600nm and 450nm are selected for comparison. An enlarged picture of specular part between 180° and 185° is also involved. Selected incident angles are indicated in Figure 4.23.

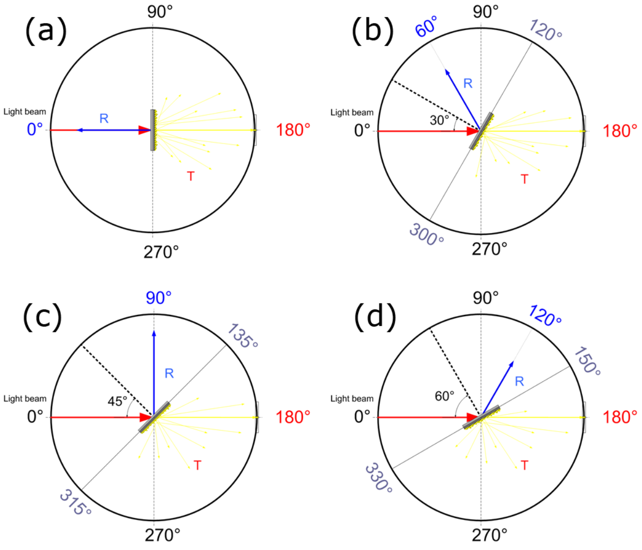

Figure 4.23: The schematic cross section of ARTA chamber along the measuring plane. Several incident angles: (a) 0 degree (b) 30 degrees (c) 45 degrees and (d) 60 degrees are used and indicated in the figure.

4.2.2.2 Aluminum doped zinc oxide

For both TCOs, the peaks of the reflected light are at the expected positions, while the peak of specular transmitted light remains at 180°, as illustrated in Figure 4.23. From Figure 4.22 and Figure 4.24, we observe a slight shift of the R_{spec} peak towards higher angles, and this effect is more pronounced for 60° incidence than 30°. This is due to multiple reflections occurring at the interfaces or within the layer which has a non neglectable thickness. As the incident angle becomes larger, a stronger *optical path difference* (OPD) occur on the reflected light, as shown in Figure 4.25(a), hence the strongest spot of reflected light is detected at a slightly higher angle. Another reason to explain this effect would be that the angular dependency of scattering properties is less accurate for light incident angles larger than 45% in the ARTA system [36], thus even more enlarge the shift of R_{spec} peak for higher incident angles.

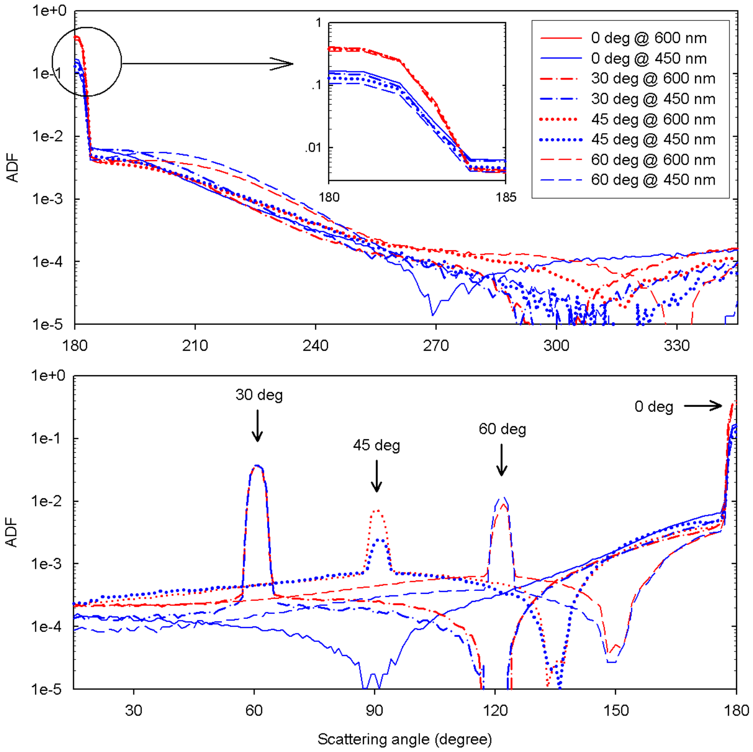

Figure 4.24: Angular distribution of transmitted (ADF_T) and reflected light (ADF_R) with different incident angle of light for AZO substrate (40-second etching). Two representative wavelengths 600nm and 450nm are selected for comparison. An enlarged picture of specular part between 180° and 185° is also involved. Selected incident angles are indicated in Figure 4.23.

For both Asahi and AZO 40-second, higher intensity of specular transmittance than reflectance are observed. This is in agreement with the result obtained in Section 4.1.1. In Figure 4.23, more light is diffused of either transmittance or reflectance for AZO 40-second, is due to its higher rms roughness than Asahi. An obvious difference between these two TCOs appears to be the intensity of R_{spec} at 45° incidence. For Asahi, the intensity of R_{spec} becomes lower with an increasing incident angle, since a stronger OPD of light results in less intensity that enter the slit of detector. While for AZO 40-second, the weakest point occurs at 45° incidence. This may be attributed to the surface morphology of AZO, which suppresses the specular reflected response at 90°. The thickness of layer may also influence the intensity of transmitted and reflected light. As shown in Figure 4.25 from (a) to (b), an increase of thickness will lead to an enhancement of light dispersion, so that more light is scattered into wide angles and the specular peak shifts. This is why a weaker intensity of scattered light for AZO which has a larger thickness is observed. The difference shown on intensities of 450-nm and 600-nm reflected light can be further explained via Fresnel's equations, in this case for p-polariztion, via Equation 2.14, but we will not go to detail here.

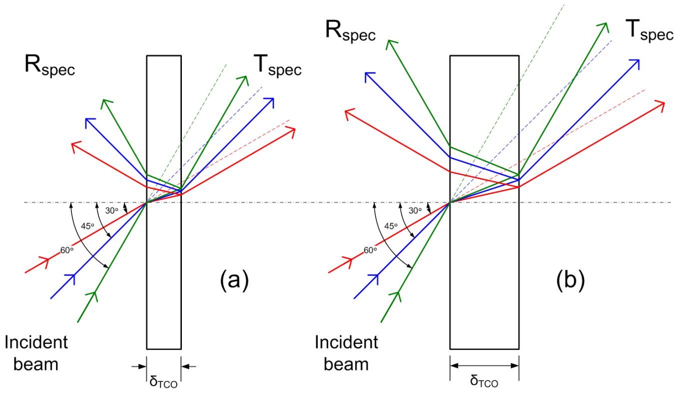

Figure 4.25: Angle shift of specular transmitted and reflected light when the thickness of TCO substrate increases from (a) relative small to (b) relative large values.

Chapter 5

Conclusions

Light trapping technique has been widely adopted in solar cells to achieve higher efficiency. In this thesis, light scattering behaviors due to different surface structures of TCO films were studied. Two optical descriptive parameters, the haze parameter and angular distribution functions (ADFs), were used to describe the light scattering properties of TCO films. While their surface morphologies were characterized by root mean square roughness (σ_{rms}). In particular, the haze parameters and ADFs were determined from measurements performed by an integrating sphere (IS) and the Automated Reflectance Transmittance Analyzer (ARTA), σ_{rms} was obtained from an Atomic Force Microscope (AFM).

Three types of TCO films were extensively investigated, including fluorine doped tin oxide (FTO), aluminum doped zinc oxide (AZO) and boron doped zinc oxide (BZO). It was shown that all TCOs exhibit high transparency (approx. 80%) in the visible region. An enhancement in light scattering was achieved when the surface rms roughness increased, and this effect was observed from either of these structures presented on the TCOs. Furthermore, light was scattered more efficiently in the shorter wavelength region, i.e. UV/Vis region. This means to achieve higher light trapping, one can propose a rough structure of which the rms roughness is more comparable to the wavelength range of interest. However, it was found that TCO films with similar rms roughness did not always deliver similar haze, and some TCOs with similar haze had different ADFs behaviors. This implies that only rms roughness is not sufficient to describe the scattering behaviors but the lateral features are required as well.

The study also demonstrated a strong correlation between ADFs and haze parameters. In general, a higher haze value corresponds to an increase in the scattered light component of the ADFs together with a decrease in the specular light component of ADFs as the wavelength becomes shorter. The variation of scattered and specular component differed from one lateral feature to another, which led to a difference in the slope of haze parameters as a function of wavelength. The angular distribution of the variation also changed, which apparently resulted in a different shape of ADFs as a function of the scattered angle.

In particular, it was showed that pyramidal (or V-shaped) structures (in this case: FTO, BZO type A and B) were more likely to scatter light into smaller angles ($180^\circ < \theta < 210^\circ$) while for crater-like surface structures (in this case: AZO), shallow angles ($210^\circ < \theta < 270^\circ$) are more favorable. For U-shaped structure (in this case: BZO type C 60-minute treatment) the light scattering behavior is more complex and is not well understood yet. An extended model to relate the surface morphology and scattering parameters still needs to be found out. With a better theoretical understanding of the scattering behaviors, one can propose optimized surface structures for future manufacturing process.

Appendix A

ARTA

To obtain a better understanding on ARTA, we include in the Appendix some facts and experience gained during various measurements performed by ARTA. The measuring setups and operating procedures are briefly described. Based on all the VAS measurements we carried out, a time rough estimation way is given, which would be helpful for future work. Some setting parameters, including integration time, PbS gain and slit width, were investigated during measurements, in order to find out suitable setups for better measuring performance.

A.1 How ARTA works

A.1.1 Measuring setup and procedure

The interfaces of spectrophotometer and ARTA *UWinLAB* and *MAC2000* are shown in Figure A.1 and A.2. In the *MAC2000* interface, the wanted range of angles and interval of angles for detector (θ_{start}, θ_{end}, $\Delta\theta$) and for sample (β_{start}, β_{end}, $\Delta\beta$) are set. The number of angles is obtained in the table, which is an input for *UWinLAB*. The number of polarizations (normally two polarizations) and samples are defined in *UWinLAB*. The main flowchart of settings are included in Figure A.1. For multiple polarization and multiple sample measurements, *UWinLAB* is instructed to perform N pairs of scans on the same sample with the polarizer, respectively, in p- and s-polarization and to perform a so-called end-of-run application after each pair before continuing with the next pair of scans [30]. Assume that sample is fixed at 0°, $\theta_{\text{start}} = 30^{\circ}$, $\theta_{\text{end}} = 90^{\circ}$ with an interval of 3. The number of sample is 3, with double polarizations, i.e. 0° for p-polarization and 90° for s-polarization. The resulted table will be shown as in Figure A.4.

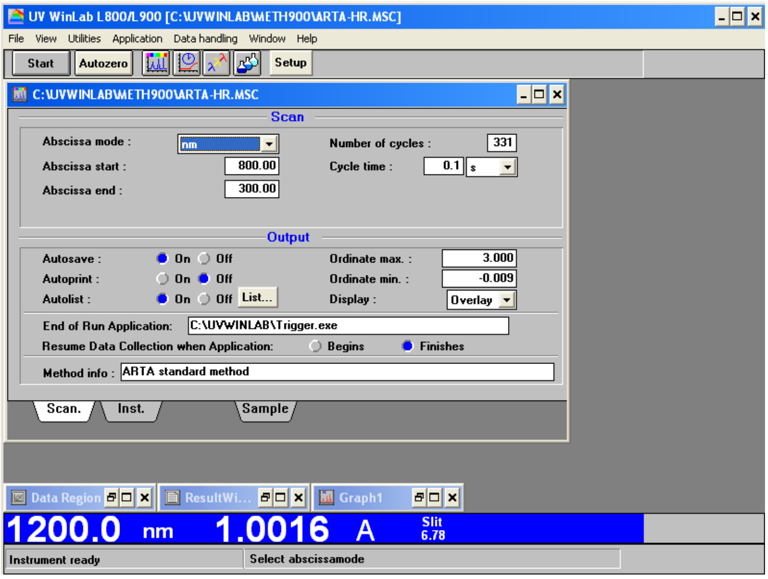

Abscissa mode : nm
Abscissa start : 800.00
Abscissa end : 300.00
Number of cycles : 331
Cycle time : 0.1 s

Autosave : ● On ○ Off
Autoprint : ○ On ● Off
Autolist : ● On ○ Off
Ordinate max. : 3.000
Ordinate min. : -0.009
Display : Overlay
End of Run Application: C:\UVWINLAB\Trigger.exe
Resume Data Collection when Application: ○ Begins ● Finishes
Method info : ARTA standard method

1200.0 nm 1.0016 A Slit 6.78

Instrument ready

Select abscissamode

Figure A.1: The spectrophotometer user interface *UWinLAB*.

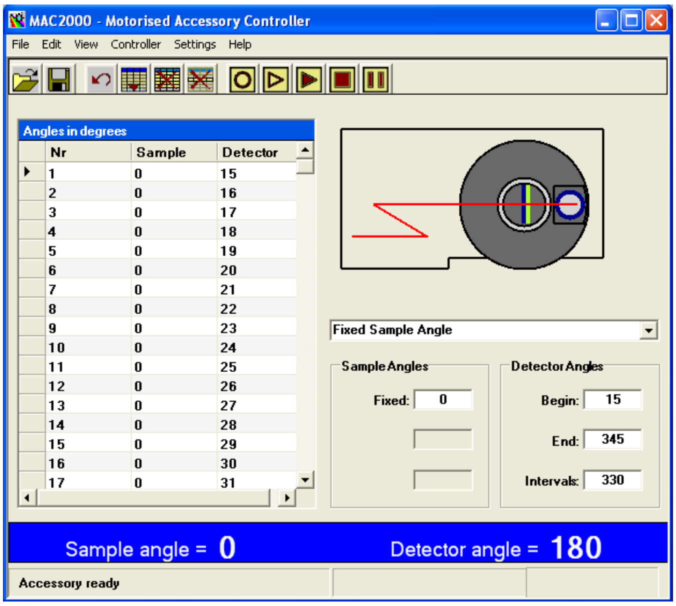

Nr	Sample	Detector
1	0	15
2	0	16
3	0	17
4	0	18
5	0	19
6	0	20
7	0	21
8	0	22
9	0	23
10	0	24
11	0	25
12	0	26
13	0	27
14	0	28
15	0	29
16	0	30
17	0	31

Fixed Sample Angle

Fixed: 0

Begin: 15
End: 345
Intervals: 330

Sample angle = 0 Detector angle = 180

Accessory ready

Figure A.2: The ARTA user interface *MAC2000*.

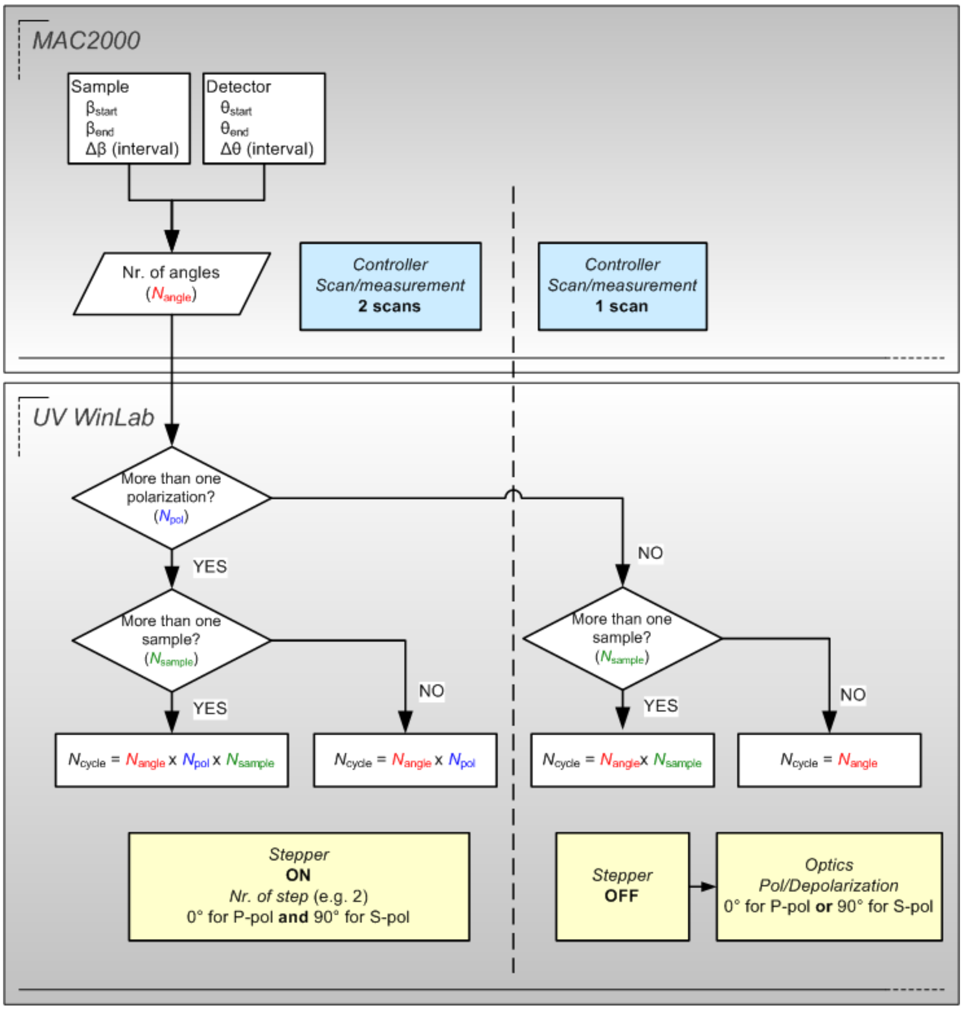

Figure A.3: The flowchart of 'number of cycle' determination.

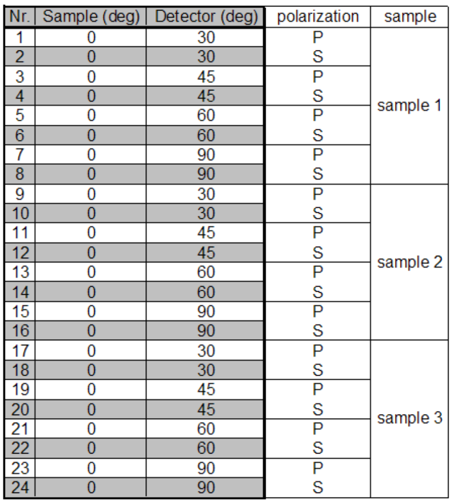

Nr.	Sample (deg)	Detector (deg)	polarization	sample
1	0	30	P	sample 1
2	0	30	S	
3	0	45	P	
4	0	45	S	
5	0	60	P	
6	0	60	S	
7	0	90	P	
8	0	90	S	
9	0	30	P	sample 2
10	0	30	S	
11	0	45	P	
12	0	45	S	
13	0	60	P	
14	0	60	S	
15	0	90	P	
16	0	90	S	
17	0	30	P	sample 3
18	0	30	S	
19	0	45	P	
20	0	45	S	
21	0	60	P	
22	0	60	S	
23	0	90	P	
24	0	90	S	

Figure A.4: An example of 'number of cycle' determination.

A.1.2 Measuring time estimation

Although an efficient measurement procedure has been developed for ARTA, when a large number of scans are required for a wide range of angles or moreover at multiple oblique incidences, these measurements are still relatively time-consuming. To make it more time efficient, it is better to estimate the time consumption for the whole measurements before start, so that one could decide whether to perform the measurements during the night, or whether some not-so-needed scans can be avoided. In this section, we extracted the time scale from 43 measurements, calculated the total time consumption and the time required to cover one scan. Results are presented in Figure A.5.

Figure A.5 shows the time consumption of ADF measurement as a function of the number of wavelength. The number of wavelength is calculated as the entire wavelength range divided by the wavelength intervals (normally 10 nm). As shown in subgraph (a), the total time spent in one measurement (all the scans of different angles) is almost linearly proportional to the number of wavelength. When the total time is divided by the number of angles, we obtained subgraph (b), which shows an exponential relationship between the time to scan all the wavelengths at one angle (one scan), and the amount of wavelengths being measured. This indicates that the more wavelengths be measured, the more time will be saved to finish one scan. As a result, if one wants to have the ADFs from 90° to 270° for only 12 discrete wavelength (e.g. 300 - 800 nm with a interval of 50 nm), then it would be wise to measure all the wavelengths continuously during the night (around 7 hours), than to change it every 40 minutes after one measurement (in total around 8 hours).

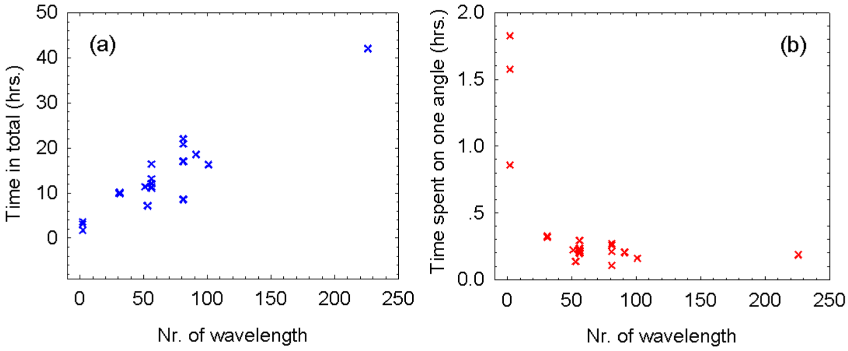

Figure A.5: The time consumption in one *ADF* measurement as a function of the number of wavelength. (a) Total time consumption (b) the time distributed into one angle with whole wavelength range.

A.2 Descriptive parameters

A.2.1 Slit width

The width of slit on the detector can be adjusted up to 30 mm. Usually $W = 1.6$ mm is used, which is corresponding to 1° shift of the detector. Different slit width varies from 1 mm to 20 mm were investigated to understand the amount of specular component of *ADF*. A relation between the slit width (W) and the angular width of specular component ($\Delta\theta_{\mathrm{spec}}$) can be derived, as expressed in Equation A.1.

$$\Delta\theta_{\mathrm{spec}} = \frac{W + W_{\mathrm{inc}}}{W_{1.6mm}}, \tag{A.1}$$

where W_{inc} is the width of incident beam (in our case approx. 10 mm by estimation) and $W_{1.6mm}$ is the distance the slit moves one degree, i.e. $W_{1.6mm} = 1.6$ mm. θ_{spec} is calculated as the angular step needed when the edge of slit first leaves the incident light beam. When $W = 1.6$ mm, we found $\Delta\theta_{\mathrm{spec}} \approx 7.2^{\circ}$. Figure A.6 illustrates the situations that W is 1.6 mm, 4 mm, 6 mm and 20 mm, respectively.

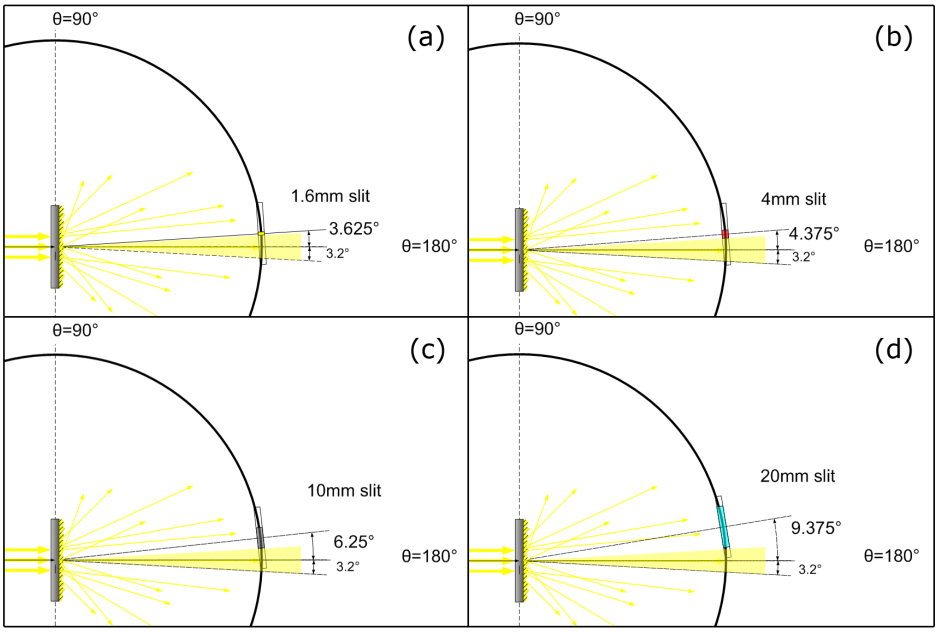

Figure A.6: Schematic cross section of ARTA chamber along the measuring plane, with detector slit width of (a) 1.6mm (b) 4mm (c) 10mm and (d) 20mm.

The ADF_T of Asahi measured with five different slit width at three representative wavelengths is shown in Figure A.7. At 800 nm, the noise decreases as the slit width is broadened, since the signal-to-noise ratio is enhanced when more light enters the slit so that higher intensity is detected. For all these wavelengths, as the slit width becomes larger, the width of the specular transmittance markedly increases. However, the diffuse component does not vary, except for $W = 20$ mm, where a significant increase is observed in the entire angle range. These observations match the result calculated from Equation A.1.

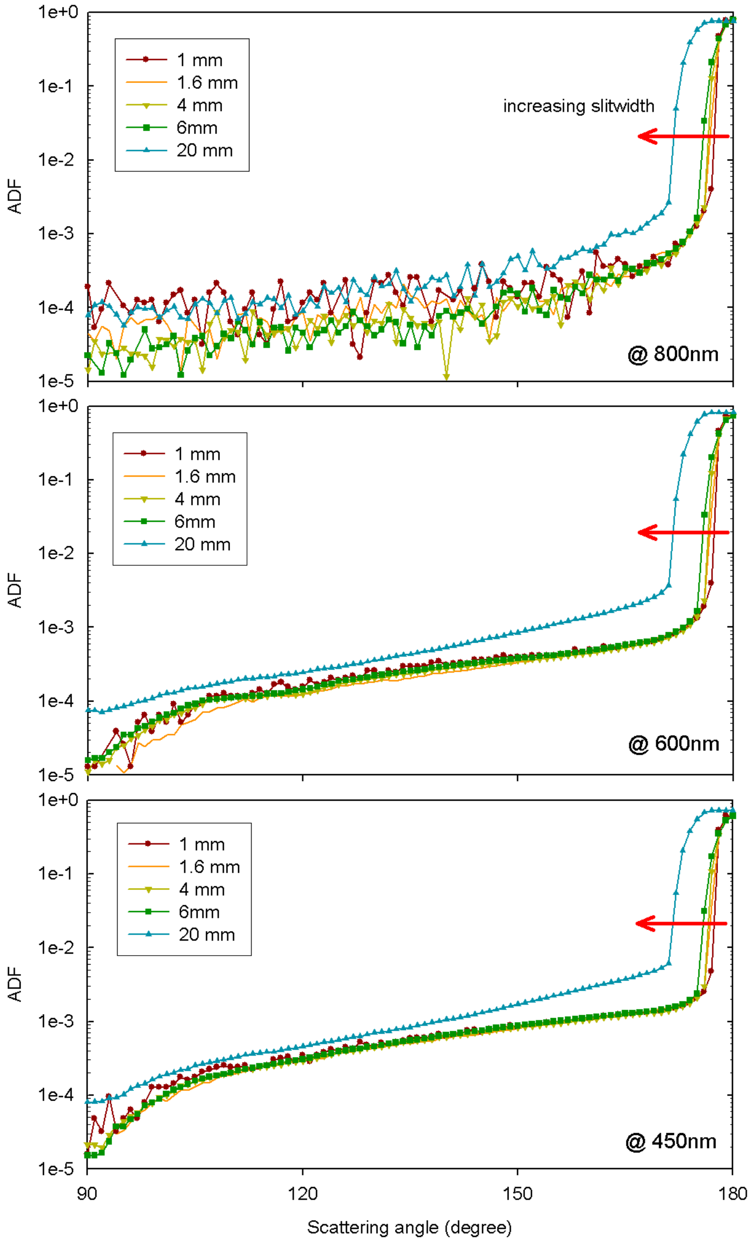

Figure A.7: ADF_T of Asahi with five different slit width at three representative wavelengths of 800nm, 600nm and 450nm.

A.2.2 Angular step

Different angular step was also used to further investigate how slit width and slit shift influence the amount of specular light received by the detector. Results are presented in Figure A.8 A.9 and A.10.

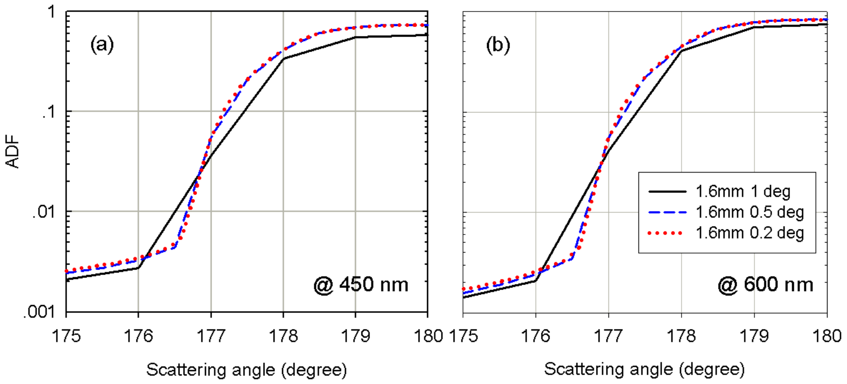

Figure A.8: Specular component of ADF of Asahi measured at $W = 1.6$ mm with different angle step. Two representative wavelengths (a) 450 nm and (b) 600 nm are selected for comparison.

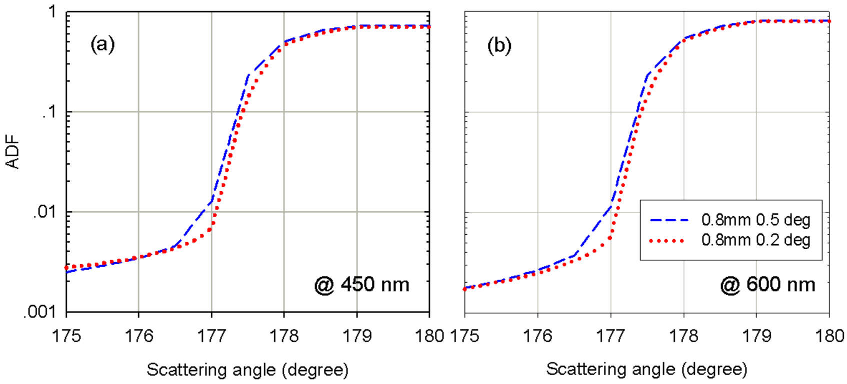

Figure A.9: Specular component of ADF of Asahi measured at $W = 0.8$ mm with different angle step. Two representative wavelengths (a) 450 nm and (b) 600 nm are selected for comparison.

In Figure A.8 and A.9, as more data points were obtained with smaller angle steps, the specular spectrum is much smoothened. This leads to an enhanced intensity of specular transmittance. With a 1.6-mm slit width, the spectrum obtained at 0.5° is very closed to the one at 0.2°, this means that with a half degree interval one can perform the measurements sufficiently accurate. 0.2° is not needed since it consumes much more time. However, this is not the case when slit width is halved, i.e. $W = 0.8$ mm. A slight difference between 0.5° and 0.2° can be observed. This indicates that an higher accurate spectrum can be achieved by using a angle step which is comparable with the width of slit, or even smaller, to ensure that every small segment of light can be received by the detector.

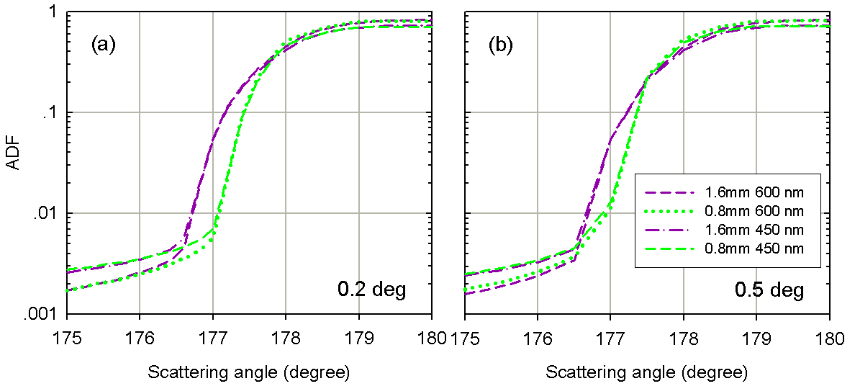

Figure A.10: Specular component of *ADF* of Asahi measured at two slit widths with a angle step of (a) 0.2° and (b) 0.5°. Two representative wavelengths are selected for comparison.

Figure A.10 shows the difference in the width of specular transmittance measured with different slit width, which is a zoom-in picture of Figure A.7.

A.2.3 Integration time and PbS gain

When the wavelength of light exceeds visible region, the ADF_T signal is too low that significant noise occurs. To minimize this effect and to gain more useful features from longer wavelength region, we expected to improve the signal-to-noise ratio by increasing the integration time and gain factor (in this case a PbS gain). Figure A.11 shows how these two parameters influence the ADF_T of an AZO sample (AZO 40-second) in the NIR region. As can be observed from subgraph (a) and (b) that, when the integration time increases from 1 second to 4 seconds, more data points can be obtained. The noise decreases markedly for all the three wavelengths. However, from subgraph (b) and (c), as the PbS gain (NIR region) is increased from 1 to 4, most of the data points are lost at both 950 and 1100 nm. This indicates that an increase of integration time will enhance the signal-to-noise ratio in NIR region, while an increase of PbS gain does not give improvement in this region, since the gain may also enlarge the noise produced by the background.

Another sample BZO type C 60-minute is investigated with same measurements and results are shown in Figure A.12. The integration time does not influence the 800 and 900-nm light in a positive way, but for 950 nm the spectrum is markedly smoothened. PbS gain gives the same impact on BZO as on AZO that, higher PbS gain leads to even more noisy *ADF* spectra. In general, increasing integration time will decrease the noise in the spectrum, but completely. Since increasing the integration time by a factor of 4 means that the total time consumption will be enormous, thus a optimum needs to be find out, to achieve higher quality of spectrum and at the same time keeps the time as short as possible.

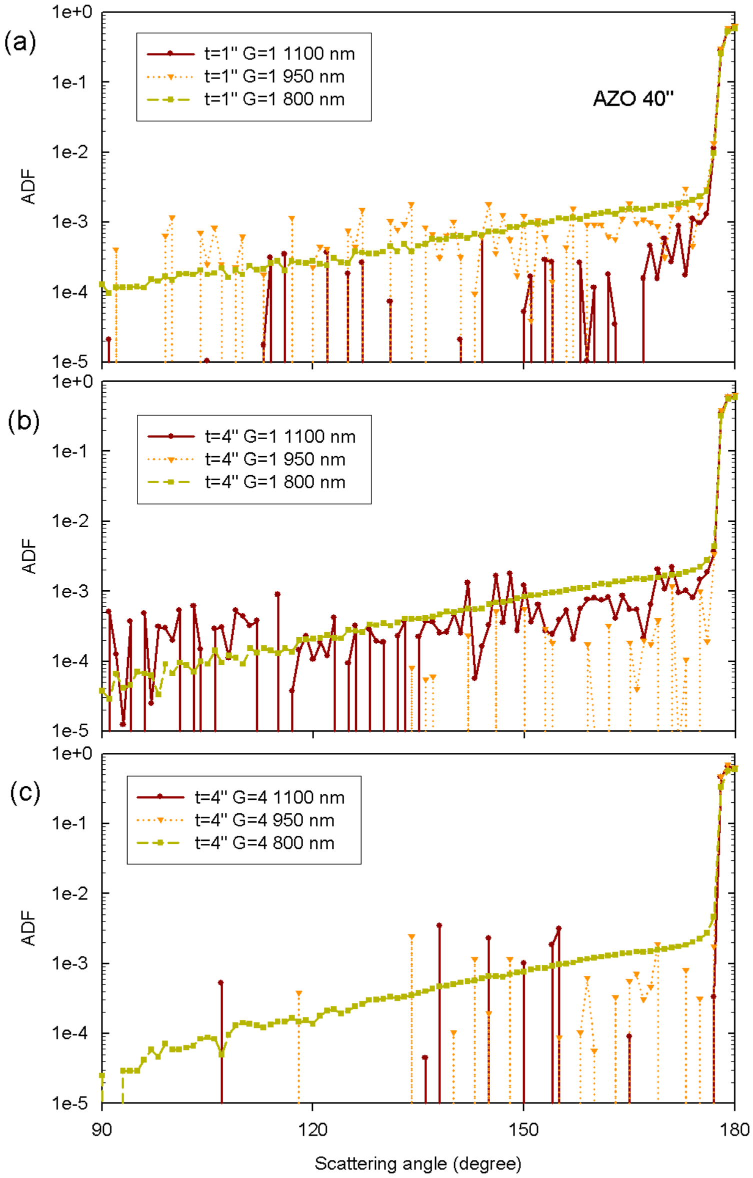

Figure A.11: The ADF_T of AZO 40-second at three representative wavelengths in the NIR region. The integration time is 1 second in subgraph (a), and 4 seconds in (b) and (c); The PbS gain for (a) and (b) is 1, while for (c) is 4.

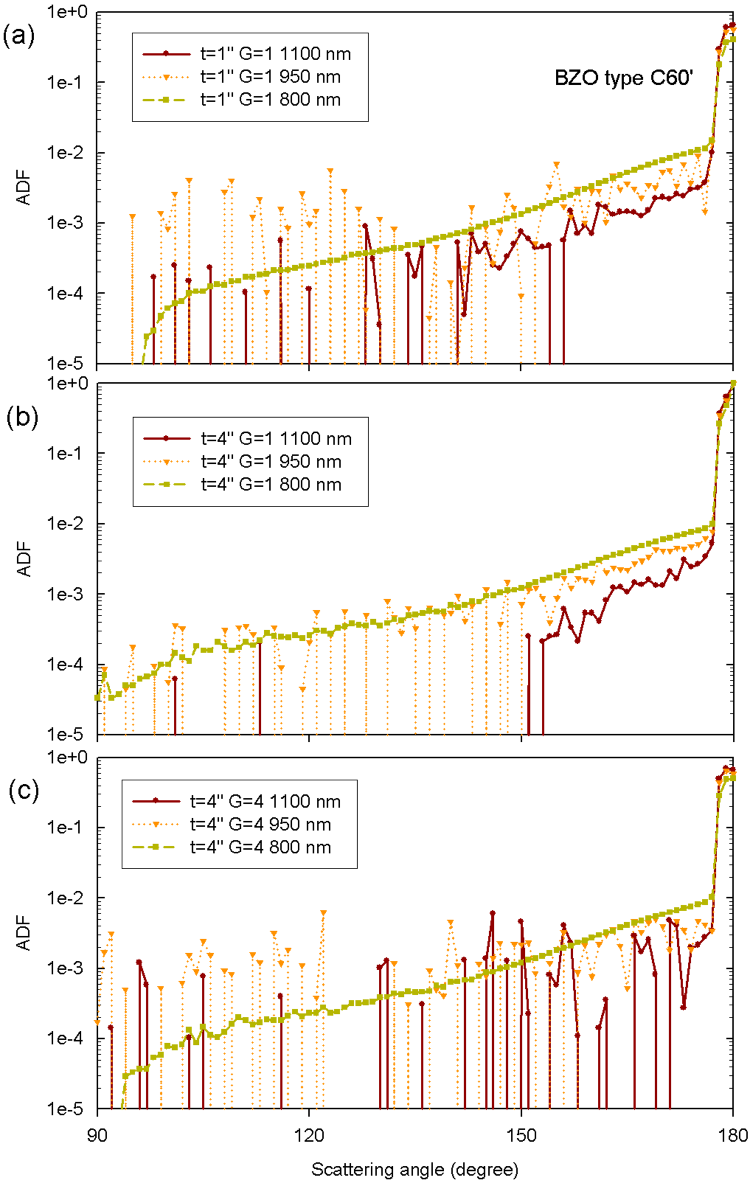

Figure A.12: The ADF_T of BZO type C 60-minute at three representative wavelengths in the NIR region. The integration time is 1 second in subgraph (a), and 4 seconds in (b) and (c); The PbS gain for (a) and (b) is 1, while for (c) is 4.

References

[1] EIA, "International energy outlook 2009," tech. rep., Energy Information Adminstration, 2009.

[2] Research and Markets, "Global solar photovoltaic market report 2008," tech. rep., Research and Markets, 2008.

[3] B. von Roedern, "Thin-film pv module review: changing contribution of pv module technologies for meeting volume and product needs," *Refocus*, vol. 7, no. 4, pp. 34 – 39, 2006.

[4] W. Spear and P. L. Comber, "Substitutional doping of amorphous silicon," *Solid State Communications*, vol. 17, no. 9, pp. 1193 – 1196, 1975.

[5] D. E. Carlson and C. R. Wronski, "Amorphous silicon solar cell," *Applied Physics Letters*, vol. 28, no. 11, pp. 671–673, 1976.

[6] G. A. N. Connell and J. R. Pawlik, "Use of hydrogenation in structural and electronic studies of gap states in amorphous germanium," *Physics Review. B*, vol. 13, pp. 787–804, Jan 1976.

[7] S. Usui and M. Kikuchi, "Properties of heavily doped gd-si with low resistivity," *Journal of Non-Crystalline Solids*, vol. 34, no. 1, pp. 1 – 11, 1979.

[8] A. Matsuda, "Formation kinetics and control of microcrystallite in [mu]c-si:h from glow discharge plasma," *Journal of Non-Crystalline Solids*, vol. 59-60, no. Part 2, pp. 767 – 774, 1983. Proceedings of the Tenth International Conference on Amorphous and Liquid Semiconductors.

[9] Y. Hattori, D. Kruangam, T. T. H. Okamoto, and Y. Hamakawa, "High efficiency amorphous heterojunction solar cell employing ecr-cvd produced p-type microcrystalline sic film," pp. 171–174, 1987.

[10] J. Meier, R. Fluckiger, H. Keppner, and A. Shah, "Complete microcrystalline p-i-n solar cell-crystalline or amorphous cell behavior?," *Applied Physics Letters*, vol. 65, no. 7, pp. 860–862, 1994.

[11] J. Meier, J. Spitznagel, U. Kroll, C. Bucher, S. Faÿ, T. Moriarty, and A. Shah, "Potential of amorphous and microcrystalline silicon solar cells," *Thin Solid Films*, vol. 451-452, pp. 518 – 524, 2004. Proceedings of Symposium D on Thin Film and Nano-Structured Materials for Photovoltaics, of the E-MRS 2003 Spring Conference.

[12] K. Yamamoto, M. Toshimi, Y. T. T. Suzuki, T. Okamoto, and A. Nakajima, "Thin film poly-si solar cell on glass substrate fabricated at low temperature," MRS Spring Meeting, San Francisco, 1998.

[13] M. A. Green, K. Emery, Y. Hishikawa, and W. Warta, "Solar cell efficiency table (version 33)," *Progress in Photovoltaics: Research and Applications*, vol. 17, pp. 85–94, 2009.

[14] K. Yamamoto, M. Yoshimi, Y. Tawada, S. Fukuda, T. Sawada, T. Meguro, H. Takata, T. Suezaki, Y. Koi, K. Hayashi, T. Suzuki,

M. Ichikawa, and A. Nakajima, "Large area thin film si module," *Solar Energy Materials and Solar Cells*, vol. 74, no. 1-4, pp. 449 – 455, 2002.

[15] M. Yoshimi, T. Sasaki, T. Sawada, T. Suezaki, T. Meguro, T. Matsuda, K. Santo, K. Wadano, M. Ichikawa, A. Nakajima, and K. Yamamoto, "High efficiency thin film silicon hybrid solar cell module on 1m2-class large area substrate," p. 1566–1569, 3rd World Conference on Photovoltaic Energy Conversion, Osaka, May 2003.

[16] K. Ellmer, A. Klein, and B. Rech, *Transparent Conductive Zinc Oxide - Basics and Applications in Thin Film Solar Cells.* Springer, 2008.

[17] R. Carius, *Structural and optical properties of microcrystalline silicon for solar cell applications*, pp. 93–108. 2002.

[18] P. Würfel, *Physics of Solar Cells: From Principles to New Concepts.* 978-3-527-40428-5, Wiley-VCH, January 2005.

[19] J. Meier, S. Dubail, S. Golay, U. Kroll, S. Faÿ, E. Vallat-Sauvain, L. Feitknecht, J. Dubail, and A. Shah, "Microcrystalline silicon and the impact on micromorph tandem solar cells," *Solar Energy Materials and Solar Cells*, vol. 74, no. 1-4, pp. 457 – 467, 2002.

[20] D. L. Staebler and C. R. Wronski, "Reversible conductivity changes in discharge-produced amorphous si," *Applied Physics Letters*, vol. 31, no. 4, pp. 292–294, 1977.

[21] D. L. Staebler and C. R. Wronski, "Optically induced conductivity changes in discharge-produced hydrogenated amorphous silicon," *Journal of Applied Physics*, vol. 51, no. 6, pp. 3262–3268, 1980.

[22] G. Tao, "Optical modeling and characterization of hydrogenated amorphous silicon solar cells," Master's thesis, Technische Universiteit Delft, 1994.

[23] S. J. AE, "Multiple internal reflection structure in a silicon detector which is obtained by sandblasting," 1969.

[24] A. Shah, M. Vanecek, J. Meier, F. Meillaud, J. Guillet, D. Fischer, C. Droz, X. Niquille, S. Faÿ, E. Vallat-Sauvain, V. Terrazzoni-Daudrix, and J. Bailat, "Basic efficiency limits, recent experimental results and novel light-trapping schemes in a-si:h, [mu]c-si:h and 'micromorph tandem' solar cells," *Journal of Non-Crystalline Solids*, vol. 338-340, pp. 639 – 645, 2004. Proceedings of the 20th International Conference on Amorphous and Microcrystalline Semiconductors.

[25] F. Meillaud, A. Shah, C. Droz, E. Vallat-Sauvain, and C. Miazza, "Efficiency limits for single-junction and tandem solar cells," *Solar Energy Materials and Solar Cells*, vol. 90, no. 18-19, pp. 2952 – 2959, 2006. 14th International Photovoltaic Science and Engineering Conference.

[26] E. Yablonovitch and G. D.Cody, "Intensity enhancement in textured optical sheets for solar cells," in *IEEE Transactions on Electron Devices*, vol. ED-29, pp. 300–305, February 1982.

[27] C. Walker, R. E. Hollingsworth, and A. Madan, "Determination of the efficiency enhancement due to scattering from rough tco contact for a-

si:h p-i-n solar cells," in *Amorphous Silicon Semiconductors - Pure and Hydrogenated* (M. A., T. M., and A. D., eds.), pp. 527–532, Materials Research Society, 1987.

[28] M. Young, *Optics and Lasers: Including Fibers and Optical Waveguides.* Springer, 5th ed., 2000.

[29] O. Stenzel, *The Physics of Thin Film Optical Spectra.* Springer, 2005.

[30] P. A. van Nijnatten, "An automated directional reflectance/transmittance analyser for coating analysis," *Thin Solid Films*, vol. 442, no. 1-2, pp. 74 – 79, 2003. Selected papers from the 4th International Conference on Coatings on Glass.

[31] H. E. Bennett and J. O. Porteus, "Relation between surface roughness and specular reflectance at normal incidence," *J. Opt. Soc. Am.*, vol. 51, no. 2, pp. 123–129, 1961.

[32] K. Jaeger, "A conversion function for arta." Private communications, 2009.

[33] J. Krc. PhD thesis, University of Ljubljana, 2002.

[34] M. G. Hutchins, A. J. Topping, C. Anderson, F. Olive, P. van Nijnatten, P. Polato, A. Roos, and M. Rubin, "Measurement and prediction of angle-dependent optical properties of coated glass products: results of an inter-laboratory comparison of spectral transmittance and reflectance," *Thin Solid Films*, vol. 392, no. 2, pp. 269 – 275, 2001.

[35] J. Krc, F. Smole, and M. Topic, "Potential of light trapping in microcrystalline silicon solar cells with textured substrates," *Progress in Photovoltaics: Research and Appllications*, vol. 11, pp. 429–436, 2003.

[36] P. A. van Nijnatten and I. J. E. Schoofs, *Absolute Directional Reflectance Transmittance Analyser.* TNO Science and Industry, July 2007.

[37] K. Bädeker, "Über die elektrische leitfähigkeit und die thermoelektrische kraft einiger schwermetallverbindungen (the electrical conductivity and thermoelectric power of some heavy metal compounds)," *Ann. Phys. (Leipzig)*, vol. 22, pp. 749–766, 1907.

[38] H. W. Deckman, C. R. Wronski, H. Witzke, and E. Yablonovitch, "Optically enhanced amorphous silicon solar cells," *Applied Physics Letters*, vol. 42, no. 11, pp. 968–970, 1983.

[39] H. L. Hartnagel, A. L. Dawar, A. K. Jain, and C. Jagadish, *Semiconducting Transparent Thin Films.* Institute of Physics Publishing, 1995.

[40] J. Hu and R. G. Gordon, "Deposition of boron doped zinc oxide films and their electrical and optical properties," *Journal of The Electrochemical Society*, vol. 139, no. 7, pp. 2014–2022, 1992.

[41] W. Beyer, J. Hüpkes, and H. Stiebig, "Transparent conducting oxide films for thin film silicon photovoltaics," *Thin Solid Films*, vol. 516, no. 2-4, pp. 147 – 154, 2007.

[42] F. Stedile, B. D. B. Jr., C. Leite, F. F. Jr., I. Baumvol, and W. Schreiner, "Characterization of tin oxide thin films deposited by

reactive sputtering," *Thin Solid Films*, vol. 170, no. 2, pp. 285 – 291, 1989.

[43] M. Ruske, G. Bräuer, J. Pistner, U. Pfäfflin, and J. Szczyrbowski, "Properties of sno2 films prepared by dc and mf reactive sputtering," *Thin Solid Films*, vol. 351, no. 1-2, pp. 146 – 150, 1999.

[44] D. Belanger, J. P. Dodelet, B. A. Lombos, and J. I. Dickson, "Thickness dependence of transport properties of doped polycrystalline tin oxide films," *Journal of The Electrochemical Society*, vol. 132, no. 6, pp. 1398–1405, 1985.

[45] E. Shanthi, V. Dutta, A. Banerjee, and K. L. Chopra, "Electrical and optical properties of undoped and antimony-doped tin oxide films," *Journal of Applied Physics*, vol. 51, no. 12, pp. 6243–6251, 1980.

[46] E. Shanthi, A. Banerjee, V. Dutta, and K. L. Chopra, "Electrical and optical properties of tin oxide films doped with f and (sb+f)," *Journal of Applied Physics*, vol. 53, no. 3, pp. 1615–1621, 1982.

[47] A. Goetzberger and C. Hebling, "Photovoltaic materials, past, present, future," *Solar Energy Materials and Solar Cells*, vol. 62, no. 1-2, pp. 1 – 19, 2000.

[48] B. Thangaraju, "Structural and electrical studies on highly conducting spray deposited fluorine and antimony doped sno2 thin films from sncl2 precursor," *Thin Solid Films*, vol. 402, no. 1-2, pp. 71 – 78, 2002.

[49] F. Simonis, M. van der Leij, and C. Hoogendoorn, "Physics of doped tin dioxide films for spectral-selective surfaces," *Solar Energy Materials*, vol. 1, no. 3-4, pp. 221 – 231, 1979.

[50] S. Munnix and M. Schmeits, "Surface electronic structure of sno2(110)," *Solid State Communications*, vol. 43, no. 11, pp. 867 – 871, 1982.

[51] Z. Zhao, M. Vinson, T. Neumuller, J. McEntyre, F. Fortunato, A. Hunt, and G. Ganguly, "Transparent conducting zno:al films via ccvd for amorphous silicon solar cells," in *Conference record of the Twenty-ninth IEEE photovoltaic specialists conference*, May 2002.

[52] X. Chen, B. Xu, J. Xue, Y. Zhao, C. Wei, J. Sun, Y. Wang, X. Zhang, and X. Geng, "Boron-doped zinc oxide thin films for large-area solar cells grown by metal organic chemical vapor deposition," *Thin Solid Films*, vol. 515, no. 7-8, pp. 3753 – 3759, 2007.

[53] B. J. Lokhande, P. S. Patil, and M. D. Uplane, "Studies on structural, optical and electrical properties of boron doped zinc oxide films prepared by spray pyrolysis technique," *Physica B: Condensed Matter*, vol. 302-303, pp. 59 – 63, 2001.

[54] J. Krc, M. Zeman, F. Smole, and M. Topic, "Optical modeling of a-si:h solar cells deposited on textured glass/sno2 substrates," *Journal of Applied Physics*, vol. 92, no. 2, pp. 749–755, 2002.

[55] W. W. Wenas, A. Yamada, M. Konagai, and K. Takahashi, "Textured zno thin films for solar cells grown by metalorganic chemical vapor deposition," *Japanese Journal of Applied Physics*, vol. 30, no. Part 2,

No. 3B, pp. L441–L443, 1991.

[56] D. Dominé, P. Buehlmann, J. Bailat, A. Billet, A. Feltrin, and C. Ballif, “Optical management in high-efficiency thin-film silicon micromorph solar cells with a silicon oxide based intermediate reflector,” *Physica status solidi (RRL) - Rapid Research Letters*, vol. 2, pp. 163–165, August 2008.

[57] J. Bailat, D. Dominé, R. Schlüchter, J. Steinhauser, S. Faÿ, F. Freitas, C. Bücher, L. Feitknecht, X. Niquille, T. Tscharner, A. Shah, and C. Ballif, “High-efficiency p-i-n microcrystalline and micromorph thin film silicon solar cells deposited on lpcvd zno coated glass substrates,” in *Conference Record of the 2006 IEEE 4th World Conference on Photovoltaic Energy Conversion*, vol. 2, pp. 1533–1536, 2006.

[58] R. W. Wood, *Physical Optics.* The Macmillan Company, New York, 1934.

[59] C. K. Carniglia, “Scalar scattering theory for multilayer optical coatings,” *Optical engineering*, vol. 18, pp. 104–115, 1979.

List of Figures

List of Tables

List of Abbreviations

μc-Si:H	hydrogenated microcrystalline silicon
a-Si:H	hydrogenated amorphous silicon
ADF	Angular Distribution Function
AFM	Atomic Force Microscopy
ARTA	Automated Reflectance Transmittance Analyzer
CVD	chemical vapor deposition
FTO	fluorine doped tin oxide
IS	Integrating Sphere
NIR	near infrared
OPD	optical path difference
QE	quantum efficiency
TCO	Transparent Conductive Oxide
VAS	Variable Angle Spectroscopy

Acknowledgments

Finally I arrive at this page. I start feeling that writing is no longer a difficult thing since I have too much to say in this part.

First, I would like to thank my supervisor Prof. Miro Zeman. From his vivid lecture I found my interest in solar cells and from him I got an opportunity to do my master thesis in the PVMD group.

Many thanks to Dr. Rene A.C.M.M van Swaaij and my previous SIP project supervisor Stefan Luxembourg, who also help me a lot to find a proper subject for my thesis.

Also I would like to show my appreciation on Prof. Fokko Mulder and Dr. Rene A.C.M.M van Swaaij, who like to be members of my Thesis Committee, and read my thesis work.

Great thanks to my daily supervisor Klaus Jäger, who helped me through every small part of my thesis work. I learned from him not only with my thesis work, but also his creative mind and optimistic attitude towards difficulties. His solid physical and mathematical background gave me great impression. Every time I encountered mathematical problems, he would guide me patiently until I understood. From him I also learned several new ways to make the job more scientific, such as using Latex, Jabref, etc. which would be very helpful in my future career.

Thanks to Olindo Isabella, who very patiently gave me the introduction on how to use IS and ARTA, the most important equipment during thesis work. Also thanks to Kasper H. Zwetsloot for his assistance on these equipment whenever I encountered problems.

Thanks to Johan van der Cingel, who helped me a lot on how to operate AFM.

Thanks to Dr. Janez Krc, for his inspiring discussions.

Thanks to Dr. Renrong Liang, for his helpful discussion and assistance.

Thanks to Folkert Moll, who deposited AZO samples for me.

Thanks to Sten Vollebregt, who gave me a lot of help on Latex.

Thanks to Jia Wei, Yujian Huang, Yuting Xu, who helped me on Matlab programming.

Also great thanks to my parents, my grandmother, my cousin sister in Delft and my friends in China, who always support me and encourage me whenever I need help.

And, I should also thank the coffee machine in DIMES building, without whom I can not survive.

Finally I would like to thank all my officemates and friends, David, Chimdi, Sten, Lijing, Folkert, Liang and Arash. I will never forget all the happy and difficult times we went through together!